Dissolution precipitation creep as a process for the strain localisation in mafic rocks

Amicia L. Lee[1*], Holger Stünitz[1, 2], Mathieu Soret[2], Matheus Ariel Battisti[3]

[*]*amicia.lee@uit.no*

[1]*Department of Geosciences, UiT – Arctic University of Norway, Norway*

[2]*Institut des Sciences de la Terre (ISTO), Université d´Orléans, France*

[3]*Instituto de Geociências, Universidade Federal do Rio Grande do Sul, Brazil*

Abstract

The lower crust is, on average, mafic in composition and composed of minerals that remain mechanically strong up to high temperatures. Here we show that dissolution-precipitation creep (as a type of diffusion creep) plays a major role in deformation of gabbro bodies at upper amphibolite facies conditions. The Kågen gabbro, N. Norway, is comprised of undeformed gabbro lenses enclosed by mylonitised margins that deformed at 690 ± 25 °C and 1.0 to 1.1 GPa. The evolution of the microstructures and fabric of the low strain gabbro to high strain margins were investigated. Original clinopyroxene and plagioclase dissolved during mineral reactions and precipitated as new minerals phases: new plagioclase and clinopyroxene (different compositions relative to the magmatic parents) and additional amphibole and garnet. Microstructural and crystallographic preferred orientation (CPO) data indicate that dissolution-precipitation creep is the dominant deformation mechanism. Amphibole shows a strong CPO that is primarily controlled by orientated growth in the stretching direction. The progression of mineral reactions and weakening is directly connected to a fluid-assisted transformation process that facilitates diffusion creep deformation of strong minerals at far lower stresses and temperatures than required by dislocation creep. Initially strong lithologies can become weak, provided that reactions proceed during deformation.

1. Introduction

Strain localisation and fabric development in the lower continental and oceanic crust are controlled by the active deformation mechanisms. The lower continental and oceanic crust are, on average, mafic in composition and primarily composed of plagioclase, pyroxene and/or amphibole (Rudnick & Fountain 1995), minerals that have been shown experimentally to remain mechanically strong up to high temperatures (Mauler *et al.* 2000, Bystricky & Mackwell 2001, Rybacki & Dresen 2004, Moghadam *et al.* 2010). Understanding the mechanisms of such deformation is the prerequisite to quantify the stresses, rates of deformation processes, and to infer general conditions and environment of the tectonic setting of lower crustal rocks.

Viscous deformation in the crust occurs primarily by two mechanisms; (1) dislocation creep and (2) diffusion creep combined with grain boundary sliding (GBS; e.g. Poirier 1985, Jessell 1987, Drury & Urai 1990, Wheeler 1992, Berger & Stünitz 1996). Dislocation creep involves intracrystalline deformation, where dislocations move through the crystal structure by processes of glide. Climb is required to minimise the internal strain energy resulting from dislocation glide (Carter & Ave'Lallemant 1970, van Roermund & Lardeaux 1991, Platt & Behr 2011). The process of diffusion creep is the result of solid-state diffusion of atoms (diffusive mass transfer) through a crystal lattice, termed Nabarro-Herring creep, or along grain boundaries, termed Coble creep (Poirier 1985, Wheeler 1992, Langdon 2006). If diffusion is combined with dissolution in and precipitation from an aqueous fluid, pressure solution allows material to be transported along grain boundaries in a fluid film rather than the movement of atoms and vacancies (Rutter 1983). Coble creep and pressure solution are efficient processes at lower temperatures than Nabarro-Herring creep and are far more likely to be dominant in crustal materials (Elliott 1973, Poirier 1985). Dissolution-precipitation creep (DPC) is a term generally used for the process of dissolving and precipitating material during diffusion creep. DPC can occur within a single phase or it may be accompanied by metamorphic reactions. In the latter case the material is precipitated as new phase(s), resulting in transformation weakening (Stünitz 1993, Okudaira *et al*. 2015, Marti *et al*. 2017, Stünitz *et al*. 2020, Mansard *et al.* 2020a).

Amphibole and plagioclase are common mid to lower crustal minerals and as a consequence they are considered to play a large role in controlling the strength of crustal scale structures (Rudnick & Fountain 1995, Tatham *et al.* 2008, Lloyd *et al.* 2011). The strength and active deformation mechanisms of plagioclase at mid to lower crustal conditions have been the subject of many studies (e.g. Marshall & McLaren 1977, Tullis 1983, Dimanov *et al.* 1999, Kruse *et al.* 2001, H. Stünitz *et al.* 2003, Rybacki & Dresen 2004, Terry & Heidelbach 2006, Miranda *et al.* 2016), yet the rheology of mafic minerals have received little attention so far (Bystricky & Mackwell 2001, Dimanov *et al.* 2003, 2011, Dimanov & Dresen 2005, Moghadam *et al.* 2010), and that of amphibole remains poorly understood.

Experimentally, amphibole is considered to be strong at lower crustal conditions (Brodie and Rutter, 1985; Shelley, 1994), and only exhibits weakening with mechanical twinning and dislocation glide at high stresses and strain rates (Rooney *et al.* 1970, 1975, Dollinger & Blacic 1975, Morrison-Smith 1976, Hacker & Christie 1990). Amphibole exhibits a fabric during diffusion creep and reaction (Getsinger and Hirth 2014). Naturally deformed amphiboles have been shown to display brittle deformation at greenschist to amphibolite facies conditions (Allison & La Tour 1977, Brodie & Rutter 1985, Nyman *et al.* 1992, Stünitz 1993, Babaie & La Tour 1994, Imon *et al.* 2004, Soret *et al.* 2019). Evidence for crystal plasticity has been interpreted (often based upon CPO) in natural samples at temperatures from 450 to >650°C via dynamic recrystallization, dislocation creep on (100)[001] and subgrain formation by dislocation glide (Biermann & van Roermund 1983, Cumbest *et al.* 1989, Skrotzki 1992, Siegesmund *et al.* 1994, Díaz Aspiroz *et al.* 2007, Pearce *et al.* 2011). Additionally, evidence for diffusion creep of natural amphibole has been inferred by dissolution-precipitation creep and/or diffusion-accommodated GBS forming strong fabrics at upper greenschist to upper amphibolite facies conditions (Berger & Stünitz 1996, Imon *et al.* 2002, 2004, Okudaira *et al.* 2015, Giuntoli *et al.* 2018, Soret *et al.* 2019, Graziani *et al.* 2020, Mansard *et al.* 2020a, 2020b). Naturally deformed amphibole usually produces strong fabrics and is thought to be responsible for the strongly anisotropic lower crust (Mainprice & Nicolas 1989, Tatham *et al.* 2008, Lloyd *et al.* 2011, Ji *et al.* 2013).

From the short summary of literature results above, it emerges that the relationships between chemical reactions, fabric formation, and deformation mechanisms in mafic rocks are poorly understood, yet they play a major role for understanding the mechanical strength of the crust and for localizing deformation in different tectonic settings. In this study, we analyse the microstructures and chemistry of the deformed margin of the Kågen gabbro (N. Norwegian Caledonides) to show the influence of mineral reactions and fluids on active deformation mechanisms and strain localisation during deformation at amphibolite facies conditions.

2. Geological setting

The Caledonides formed from convergence and collision of Baltica and Laurentia during the Silurian to Devonian periods. In northern Norway, large-scale nappe stacking preserves a section of autochthonous Baltica basement and ophiolites with varying metamorphic grades and deformation style (Corfu *et al.* 2014). The Reisa Nappe Complex (from bottom to top: Vaddas, Kåfjord, and Nordmannvik nappes; Figure 1a) in northern Troms is considered to be Iapetus-derived or part of the outer Baltica margin (Andersen *et al.* 1982, Corfu *et al.* 2006). It underwent viscous deformation and metamorphism at amphibolite- to granulite-facies conditions with pervasive partial melting (Roberts & Sturt 1980, Faber *et al.* 2019).

The Kågen gabbro intruded into amphibolite to granulite-grade metasediments of the Vaddas Nappe and is exposed on the islands of Kågen and Arnøya (Figure 1b). The emplacement of the gabbro occurred at 439±1 Ma (U-Pb zircon concordia age; Faber *et al.* 2019), and cooling is recorded over a broad temperature range of 650-900°C at pressures of 0.7-0.9 GPa that correspond to depths of 26-34 km resulting in partial melting of the adjacent felsic and metapelitic rocks (Getsinger *et al.* 2013, Gasser *et al.* 2015, Faber *et al.* 2019). A mantle melt source and extensional setting is implied from the tholeiitic composition of the gabbro in the Vaddas Nappe (Lindahl *et al.* 2005).

The sample location is situated near the western margin of the Kågen gabbro on Arnøya (GR: 70.04389N, 20.71444E). The outcrop region consists of undeformed gabbro lenses with mylonitised margins enveloping the lenses (Figure 2a), and is approximately 0.7 km west of samples studied by Getsinger *et al.* (2013). The area studied by Getsinger *et al.* (2013) hosts several hydrous pegmatite intrusions that locally hydrated the gabbro and partitioned deformation during emplacement of the gabbro. The deformed margins of gabbro pods in our sample area are not associated with pegmatite intrusions, and, together with the formation of a regional fabric close to margin of the gabbro body, indicate a different setting for the deformation.

The Vaddas Nappe underwent shearing at 432±6 Ma (TIMS, mean ^{206}Pb/^{238}U age in titanite), temperatures of 630-640°C, pressures of 1.2-1.3 GPa and depths 43-46 km during the main Scandian collision event of the Caledonides (Faber *et al.* 2019), and the gabbro outcrops of this study have been deformed during this orogenic stage. This paper investigates the processes occurring during deformation of mafic rocks and where the observed deformation in the Kågen gabbro is related to the Vaddas Nappe and Caledonian deformation history.

3. Methods of study

In this paper we analysed polished thin sections in order to investigate the features of strain variation through sample A8B described below (Figure 2c, Table 1). The sample is cut in the X-Z section of the kinematic reference frame. Where minerals have been abbreviated, we follow the database from Whitney & Evans (2010).

3.1 *Electron microscopy*

Electron probe microanalysis was carried out at CAMPARIS (Sorbonne University, Paris, France) using a Cameca SX-Five instrument. Point measurements were made using 15 kV accelerating voltage, a 10 nA beam current with a 1 µm spot size. Composition maps were acquired using a 15 kV accelerating voltage, a 40 nA beam current with a 1 µm spot size and 50 ms dwell time. The instrument was calibrated using diopside (Ca, Mg, Si), MnTiO3 (Mn, Ti), orthoclase (K, Al), Fe2O3 (Fe), albite (Na) and Cr2O3 (Cr) as standards to measure elements in brackets. Selected representative analyses of garnet, clinopyroxene, plagioclase and amphibole from point analysis are shown in Table 2.

3.2 *Thermodynamic modelling and empirical thermo-barometry*

Several empirical thermo-barometers were used to estimate the pressure-temperature conditions of formation of the mineral assemblages observed in the low, mid and high strain zones. The crystallization temperatures of metamorphic garnet and clinopyroxene pairs at microstructural equilibrium were estimated using the thermometer of Powell (1985). For these estimates, pressure was taken to be ~1 GPa - a conservative assumption as garnet–clinopyroxene thermometry is poorly dependent on pressure (pressure variations of 0.5 GPa affect the temperature by ≤ 15°C). The crystallization temperatures of amphibole and plagioclase pairs were calculated using the combined thermo-barometers of Holland & Blundy (1994) and Molina *et al.* (2015).

In addition, forward thermodynamic modelling (Perple_X software version 6.8.6; (Connolly & Kerrick 1987, Connolly 2009) were conducted to estimate the pressure-temperature conditions of the high strain layers. In contrast to the low and mid strain domains, the high strain domain showed clear criteria of chemical equilibrium. The pseudosection was modelled in the NCKFMASH system using the internally consistent thermodynamic dataset (hp62ver.dat) of Holland & Powell, (2011). The following solution models were used: White *et al.* (2014) for orthopyroxene, biotite, chlorite and garnet, Green *et al.* (2016) for mafic melts, augite and hornblende, and Holland & Powell (2003) for plagioclase and K-feldspar. The H_2O value was set to 1.1 wt. % after calculating a T-X(H_2O) diagram with a H_2O content ranging from 0.5 to 2 wt.% (i.e., excess water) at a pressure of 1 GPa, consistent with the estimates from the amphibole-plagioclase thermo-barometry (Figure S1, Table S1; Holland & Blundy 1994, Molina *et al.* 2015). The H_2O value is also consistent with the proportion of amphibole (~ 50 vol. %) observed in the high strain layers (see section 4.1.3).

3.3 Electron backscattered diffraction (EBSD)

Crystallographic orientation data was collected via electron backscattered diffraction (EBSD) Oxford Instruments Nordlys S detector also on the Zeiss Merlin SEM at the University of Tromsø. Crystallographic data were collected using 20 kV accelerating voltage, 70° specimen tilt angle and 24-29 mm working distance. Detailed maps of ~16 mm^2 were measured with a step size of 1-3 µm and 7 bands detected. Oxford Instruments Aztec software was used for data acquisition and initial data processing, MTEX v.5.2.8 open source software toolbox (Bachmann *et al.* 2010) for MATLAB was used for enhanced data processing and pole figure plotting. Individual crystal orientations with median absolute deviation (MAD) values >1.0 were removed. Individual grains were reconstructed using the ‘calcGrains’ function in MTEX using a 10° misorientation cut-off relative to neighbouring solutions. Pole Figures were created for the mean orientation of each grain based on the orientation distribution function (ODF), using the ‘calcDensity’ function within MTEX (Bachmann *et al.* 2010). The mean orientation of each individual grain was then plotted on lower hemisphere, equal area pole figures such that each data point represents a single grain on the pole figure, which are subsequently contoured. Calculated J-indices show the CPO fabric strength (e.g. e.g. Bunge 1982, Mainprice and Silver, 1993) and the M-indices shows the misorientation index (e.g. Skemer *et al.,* 2005).

3.4 Grain shape parameters

Grain size and shape parameters are measured using grains calculated from the EBSD map data as described above with a misorientation threshold of 10°. The grain size is calculated via the equivalent radius (derived from the grain area) and multiplied by 2 to yield the grain size. The grain data for low, mid and high strain areas have been grouped together to give an overview of grain shape parameters in each of the strain zones (see Table 1 for strain domains). The histogram has 5 µm bin sizes and shows grain sizes up to 500 µm (larger grains are present in the samples but low in quantity). Grain statistics for mean, median, mode (range of largest bin) and standard deviation are shown alongside the grain size histogram data in. Grain orientation is calculated using a fitted ellipse and orientation of the long axis.

4. Results

4.1 Sample description

The outcrop displays strain gradients with weakly deformed low strain domains (5-20 cm in height, 20-40 cm in length) that are bound by high strain mylonites (Figure 2). Even in the less deformed domains, the original gabbroic fabric described by Getsinger *et al.* (2013; c.700 m east) is not or only partially preserved (Figure 2). Mid-strain domains show segregation of mafic and plagioclase-derived minerals, and this distinction develops into thin layers in most high strain zones (Figure 2c). Below, we present the results for microstructures, chemical properties and crystallographic preferred orientation (CPO) of each type of domain (low, mid and high strain zones). Strain domains present in each thin section and EBSD map are summarised in Table 1.

The heterogeneous strain distribution typically shows the highest strain parts between lower strain parts. Such a strain distribution is interpreted as a narrowing of shear zones caused by progressive localization of deformation (type 2 shear zone; Means 1995). This interpretation implies that lower strain regions preserve earlier stages and the highest strain regions the last stages of the deformation history.

4.1.1 Low strain zones

The primary phases in the low strain zones are clinopyroxene and plagioclase with minor orthopyroxene, amphibole ilmenite and zoisite (Figure 3a). The original igneous gabbro assemblage has been metamorphosed; original pyroxene porphyroclasts (referred to as cpx_1) are surrounded by a mixing of secondary pyroxene (cpx_2) and amphibole (amp_A) grains forming corona rim structures. New plagioclase grains (pl_2) replace original plagioclase grains (pl_1; Figure 4a-c, 6c).

The cpx_1 grains are much larger in size (3-6 mm) than the cpx_2 grains (< 200 μm). The cpx_1 show undulose extinction and thin lamellae of ilmenite and amphibole reaction products (amp_A) along cpx_1 cleavage planes/cracks (Figures 3a-b, 4a-b). Some large cpx_1 grains have neo-crystallized portions that follow larger cleavage cracks in the original grain; these are composed of both cpx_2 and amp_A (Figure 4a-b).

The amp_A grains have a larger grain size in the cpx_1 strain pressure shadows, 50 vs. 100 μm (Figure 4a-f, 5a). Shape and size analysis of amphibole grains show a unimodal grain size distribution with a mean grain size of 68 μm and grains are elongated parallel to the foliation (Figure 5a, d). The orthopyroxene grains have also been replaced by amphibole; the few relicts that remain are fully recrystallized (Figure 3a).

The original pl_1 grains are up to 3 mm with undulose extinction. They generally include zoisite needles up to 400 μm in length (Figure 4b-c, 6c). The later neo-crystallized pl_2 grains are recrystallized 50-300 μm in size and show straight extinction and ~120° triple junctions (Figure 4b-c). The plagioclase domains typically appear more deformed than the pyroxene domains and form a weak foliation.

Ilmenite is found adjacent to clinopyroxene grains and often exhibits amphibole or garnet coronas rims (Figure 3a, 4d). Olivine is not found in the A8B sample, but it is present in undeformed gabbro ~700 m east as detailed by Getsinger *et al.* (2013).

4.1.2 Mid strain zones

Towards the margins of the gabbro pods, the foliation is progressively stronger in intensity (Figure 3b). Clinopyroxene, plagioclase and amphibole are the dominant phases with minor amounts of garnet, zoisite, quartz and ilmenite whilst orthopyroxene is not present. Corona structures are ubiquitous and grade into elongated tails at the ends of porphyroclasts defining the foliation.

Cpx_1 grains represent the primary grains and are 0.5-2 mm in size (smaller than in the low strain areas of the rock). The primary cpx_1 grains have undulose extinction and the thin lamellae of amp_A along cpx_1 cleavage planes can be recrystallized as ‘blebs’. The recrystallized tails consisting of new grains of cpx_3 have a granoblastic texture without signs of internal grain deformation (top right of Figures 4d, 5b-c).

The amp_A grains that surround both cpx_1 grains and cpx_2 grains from recrystallized tails are coarser than in low strain domains, up to 200 μm. Quartz is present in trace volumes between some cpx_1 grains and their surrounding amp_A rims (Figure 6c). There are zones where amphibole (amp_B) has almost completely replaced the cpx_1 (e.g. amp_{B2} zone in Figure 4f). In these elongated zones of bands the amp_B grain size is up to 500 μm. Within these bands, there are minor amounts of clinopyroxene, quartz and ilmenite. Despite the observed grain size increase in amphibole, the average grain size is only 64 μm as there is a high proportion of small amp$_A$ grains associated with the clinopyroxene replacement (cpx$_2$; Figure 4d-f, 5b).

Similarly to the cpx$_1$, the large pl$_1$ grains are smaller in the mid strain zone (up to 2 mm), although still exhibit undulose extinction and deformation bands. The recrystallized pl$_2$ grains show little internal deformation. Some grain boundaries are more lobate than in the low strain zones (Figure 4e, 6c). The amphibole and plagioclase grains in the mid strain areas are orientated with their long axes parallel to the foliation (Figure 5e). Prismatic zoisite is up to 500 µm in length within large pl$_1$ grains where they are loosely aligned to the foliation but zoisite is also present in the smaller pl$_1$ grains with a random orientation (Figure 4c, e). In some mid strain regions garnet grows in bands after cpx$_1$, pl$_1$ and ilmenite, the grains are up to 100 µm in size, are faceted and have equant shape with quartz inclusions (Figure 4d-e).

4.1.3 High strain zones

In several layers around the gabbro pods and in between the mid strain zones, there are high strain zones, where the rock is strongly deformed and appears mylonitic in the field (Figure 2). The foliation is well developed in the high strain zones exhibiting alternating bands of amphibole and plagioclase with occasional garnet bands (Figure 3c). The amp$_B$ bands have trace amounts of clinopyroxene, quartz, calcite, and ilmenite interspersed (Figure 4g-i).

The amp$_B$ grains are up to 600 µm in length with a mean grain size of 91 µm (Figure 5c). Amphibole in layers associated with garnet and ilmenite are olive green (amp$_{B1}$) in colour under plane polarized light, compared to amphibole layers with low volumes of minor minerals that are jade green (amp$_{B2}$) in colour (Figure 4g-i). Amphibole shows the strongest SPO of the differently strained zones with grains strongly orientated parallel to the shear direction, and also to the foliation (Figure 5f).

The pl$_2$ bands are recrystallized and no longer contain any of relicts of original pl$_1$ grains (porphyroclasts; Figure 4g-i). Pl$_2$ is also present in mixed bands with amp$_B$, forming polyphase layers (Figure 4i). In such layers, the mean plagioclase grain size is decreased to 83 μm and the grain size distribution is virtually identical to amphibole (Figure 5c). The plagioclase grains show a similar long axis orientation in the mid and high strain areas (Figure 5 e-f).

Quartz is present as interstitial blebs and inclusions within amphibole and plagioclase. Calcite and ilmenite are both cuspate in shape. Zoisite is rarely present in high strain zones. When found it is less than 20 μm long and randomly orientated (Figure 4h). Garnet bands up to 4 mm in width are commonly associated with amphibole-plagioclase band alternation (Figure 4g). Isolated garnet grains are also present within amphibole layers. The garnets are subhedral, typically 1-3 mm in size and are associated with quartz and calcite. Quartz is present as inclusions and interstitial blebs in the garnet whilst calcite is interstitial forming cuspate shapes around the garnets (Figure 4g, 6b).

4.2 Mineral chemistry

Clinopyroxene has a diopside-rich composition with a Mg# [Mg/(Mg+Fe)] ranging between 0.65 and 0.80 (Figure 6a, Table 2). Magmatic porphyroclasts of cpx$_1$ (samples A8B1, A8B4) show higher values (0.75-0.80) than new small cpx_2 grains at their rims and tails (0.75-0.72). New metamorphic cpx_3 grains scattered in the matrix (sample A8B4) show the lowest Mg# values (0.65-0.73). The amount of Na, representing the jadeite content, varies between 0.3 and 0.5 a.p.f.u. regardless of the microstructural position. The changes in Mg and Na content are illustrated in Figure 6a-b, new small grains surrounding or forming tails around magmatic cpx_1 porphyroclasts have lower MgO and higher Na_2O value than the original cpx_1 grains. All chemical analyses are available in Table 2.

Amphibole analyses plot within the pargasite to actinolite fields (nomenclature from Leake *et al.* 1997; Figure 7b). The Mg# varies between 0.50 and 0.75, and the Ti ranges up to 0.25 a.p.f.u (Figure 7c, Table 2). The Mg# shows a continuous increase, and the Ti a continuous decrease versus increasing Si, with clear microstructural relations (Figure 6). Amp_A crystallizing after the magmatic cpx_1 porphyroclasts in the low and mid strain zones (samples A8B1, A8B4) has the highest Mg# (> 0.60) and Si values (> 6.6 a.p.f.u.) and the lowest Ti content (< 0.1 a.p.f.u.). In the low, mid and high strain zones, amp_B co-existing with pl_2 has lower Mg# (<0.63) and Si values (<6.6 a.p.f.u) with generally higher Ti content (0.06-0.16 a.p.f.u.). While amp_C included in garnet in the mid strain zone has the same composition as amp_B in the plagioclase-rich layers, amp_D included in garnet in the high strain zone shows the highest Ti content (0.12-0.24).

The plagioclase has an anorthite content [Ca/(Ca+Na)] varying between 0.25 and 0.60 (Figure 7d). A correlation is observed with both microstructural position and fabric intensity. In the low (A8B1) and mid (A8B4) strain zone, the cores of magmatic pl_1 porphyroclasts (Figure 6a) have the highest anorthite content (0.54-0.60). The prophyroclast rims and new small grains of pl_2 at microstructural equilibrium with amp_B

in such samples (Figure 6a, c) show an intermediate composition (values of 0.35-0.55). A similar distribution is observed for the new recrystallized pl_2 grains equilibrated with amp_B in the high strain zone (e.g. mixed amp-pl bands in Figures 4h-c, 11c), varying from 0.28 to 0.45. Pl_3 in the garnet-amphibole bearing layers from the mid and high strain zones (samples A8B4, A8B9) have the lowest anorthite content (0.25-0.40).

The garnet chemical composition in the amphibole-free layers of the mid strain zones varies in function of the neighbouring minerals (Figure 6 c, 7e-f). Regions near crystal faces next to clinopyroxene are enriched in Fe and Mg (Alm: 0.59, Prp: 0.15, Grs: 0.23, Sps: 0.02) while regions near faces next to plagioclase are enriched in Ca (Alm: 0.51, Prp: 0.10, Grs: 0.36, Sps: 0.02). Mn content remains low regardless of the neighbouring minerals. Garnet in the $amp_{C/D}$-rich layers of the high-strain zones shows a more homogeneous composition (Alm: 0.53-0.57, Prp: 0.13-0.14, Grs: 0.25-0.29, Sps: 0.05) that lies in-between the two garnet compositions recognized in the mid-strain zones.

Mineral chemistry exhibits local microstructural variations within the gabbro. For example, Figures 6a-b and 7a show the variation in Mg-content between cpx_1 porphyroclasts and adjacent new cpx_2 grains. The garnet grain B in Figure 7e shows how garnet chemistry varies when adjacent either to clinopyroxene or to plagioclase. The garnet rim around a clinopyroxene grain shows a variation in Mg content (Figure 6c); when adjacent to plagioclase it is more depleted than the core which is adjacent to clinopyroxene and ilmenite. Figure 6d shows a chemical map in a high strain amphibole area and how the chemistry varies between the olive green (amp_{B1}, top) and jade green (amp_{B2}, bottom) coloured amphibole (e.g. Figure 4h-i); the olive green coloured amp_{B1} has higher Mg and Si values compared to the jade green coloured amp_{B2}. In addition the olive green coloured amp$_{B1}$ exhibits zoning, with a decreasing of Mg and Si content from core to rim.

4.3 Pressure-temperature estimates

The amphibole-plagioclase thermo-barometry (Holland & Blundy 1994, Molina *et al.* 2015) yielded results for three samples of the low, mid and high strain zones (samples A8B1, A8B4 and A8B9, respectively; Table S1). The amp$_B$-pl$_2$ pairs were chosen based on textural evidence of equilibrium: immediately adjacent analyses along straight grain boundaries. The results indicate similar P-T conditions of 690 ± 25°C and 1.05 ± 0.15 GPa for all domains (Figure 8 inset, Table S1). Crystallization temperatures in the mid strain zone were also calculated using the garnet-clinopyroxene thermometer of Powell (1985) and Krogh (1988; Table S2). Metamorphic pairs at textural equilibrium (Mg-Fe-rich garnet and cpx$_2$; Figure 6c) at textural equilibrium yielded 700 ± 25°C at 1 GPa (Figure 8 inset).

Peak P-T conditions of the high strain zone were additionally constrained through thermodynamic modelling. The best fit of the garnet, amphibole and plagioclase isopleths lie in the field with Amph + Cpx + Grt + Pl + Qz (without free-water), around 675 ± 25°C and 1.05 ± 0.05 GPa (Figure 8). The predicted mineral compositions of plagioclase, amphibole and garnet match those documented by mineral analyses in this study. The modelled temperatures and pressures are in very good agreement with those of the conventional thermo-barometry.

4.4 Crystallographic preferred orientation (CPO)

Figure 9 shows lineation-parallel (= X-pole-figure-axis) amphibole orientation maps, CPO pole figures, and inverse pole figures (IPF) of amphibole and clinopyroxene. Clinopyroxene CPO's are only shown for low and mid strain areas as there are insufficient grains in the high strain areas to construct statistically meaningful pole figures. All individual phase maps and CPO pole figures for amphibole, clinopyroxene, plagioclase, quartz, calcite and ilmenite are available in supplementary information (Figure S2-6).

In the low strain areas, amphibole CPO is characterised with poles to the (100) subnormal to the shear plane (XY-pole figure-section; Figure 9), and the [001] axes subparallel to the shear direction (X-axis). The amphibole J-index is 8.26 and the M-index is 0.284 for the example low strain zone (A8B1). The misorientation axes for amphibole subgrains (2-10°) show maxima around [001] and account for >25% of misorientations (Figure 9d). When the clinopyroxene CPO is considered alongside the amphibole CPO, the maxima are weaker but they are orientated in similar directions. The misorientation axes for clinopyroxene subgrains is very strong around [001] and accounts for 50% of the total misorientation.

In the mid strain area the amphibole CPO has a similar fabric to the low strain area; poles to the (100) plane are subnormal to the shear plane, and the [001] axes is subparallel to the shear direction (Figure 9). The [001] axes shows a weaker maximum but are aligned closer to the shear direction than the fabric in the low strain areas. For the mid strain zone, the amphibole J-index is 3.33 and the M-index is 0.111 (A8B4). The subgrain misorientation axes are weakly distributed between [001] and [-100], with the highest frequency of misorientations associated with subgrains. The clinopyroxene CPO in the mid strain areas is very weak and does not correlate to the amphibole CPO (Figure 9).

In the high strain region (A8B9), the amphibole CPO exhibits a weak girdle and maximum of poles to (100) orientated normal to the shear plane, poles to (010) planes in a weak maximum subnormal to the foliation and the shear direction and the [001] direction shows a strong maximum parallel to the shear direction (Figure 9). The amphibole J-index is 4.25 and the M-index is 0.128 for the high strain area. The amphibole subgrain misorientation axes is strong around [001] and accounts for >20% of misorientations (Figure 9d).

The relationship between the amphibole and clinopyroxene CPO is further explored in Figure 10 where four regions of a clinopyroxene grain with amphibole replacement has been studied. Region A shows the CPO for the clinopyroxene grain (cpx_1) and all surrounding amphibole grains. This amphibole CPO is weak and the maxima are directly related to maxima in the clinopyroxene CPO. Region B focusses on the left hand side of the main clinopyroxene grain ($cpx_{1/2}$), which has undergone more recrystallization than the right. The CPO is almost identical to region A, but is much stronger (for clinopyroxene and amphibole) than in region B. Region C shows the CPO for the right hand side of the clinopyroxene grain (cpx_1) and the amphibole (amp_A) inclusions within the grain. The CPO for this area is very strong, the amphibole and clinopyroxene maxima are in identical positions and are similar to the CPOs observed in regions A and B. The final area, region D, considers the tail of the clinopyroxene (cpx_2) where the highest amount of recrystallization and deformation has occurred. The clinopyroxene CPO for region D is very weak and does not bare a strong resemblance to the amphibole CPO. The amphibole CPO in region D is similar to the whole map amphibole CPO (region A) in the mid strain area in Figure 9b.

The plagioclase CPO is generally weak; in low strain regions there tends to be a very weak CPO (Figure 11a) but the CPO is not consistent between different low strain maps (see Figure S5). The high strain area was analysed in subsets to see if there is a change in CPO strength between monophase and polyphase regions (Figure 11c; e.g. Mehl & Hirth 2008). The CPO is weak and shows no fabric in any of the subsets, for plagioclase. Nevertheless, the amphibole for this (and all other) high strain areas shows a strong CPO with (001) normal to the shear direction and [001] parallel. The plagioclase CPO is also weak in the mid strain zone.

The quartz, calcite and ilmenite show disordered CPOs, they are either weak or strongly dominated by a few grains. Pole figures for these minerals are found in supplementary figures S6.

5. Discussion

The Kågen gabbro is a 45 km^2 intrusion with a relatively unaltered and undeformed core. Deformation increases towards its margins with the Vaddas Nappe. The southern coastline of Arnøya provides a transect through the gabbro. The centre of the gabbro is relatively undeformed with a clinopyroxene, olivine, and plagioclase (± orthopyroxene) assemblage (Getsinger *et al.* 2013). There is localised deformation in the core of the gabbro where it is cross-cut by fluid-rich pegmatites. The deformation in the immediate vicinity to pegmatites is related to fluid released during pegmatite emplacement, the late magmatic stage of the gabbro intrusion (Getsinger *et al.* 2013).

Towards the edges of the gabbro (best exposed in the west), lenses of weakly deformed gabbro are surrounded by high strain margins; representing a small scale version of the general strain distribution of the whole gabbro body. The deformation at the gabbro margins overprints the largely undeformed gabbro body. This suggests the centre of the gabbro did not experience deformation during this deformation phase, it remained strong and rigid, whilst heterogeneities produced by local mineral reactions at the margins were exploited to localise deformation during emplacement of the Vaddas Nappe (Getsinger *et al.* 2013, Faber *et al.* 2019).

5.1 Mineral reactions and P-T-time of deformation

Getsinger *et al.* (2013) studied intrusion related deformation within the centre of the Kågen Gabbro, and observed an assemblage similar to the low strain areas in this study. The undeformed gabbro of Getsinger *et al.* (2013) has higher volumes of olivine and clinopyroxene, and the amphibole corona rims are absent or not well developed. Clinopyroxene is the main mafic phase of the gabbro. According to Getsinger *et al.* (2013) orthopyroxene in the undeformed gabbro is commonly associated with the olivine and has formed as reaction rims around it. Therefore, it is suggested that the initial alteration of the gabbro occurred via olivine reacting with plagioclase forming pyroxene (plus some spinel) rims:

$$Pl_1 + Ol \rightarrow Cpx_1 + Opx \pm Spl. \qquad \text{(R1)}$$

Metamorphism of the margins of the Kågen gabbro likely occurred during emplacement and deformation of the Vaddas nappe. This main deformation event resulted in a pyroxene consuming and amphibole producing hydration reaction during nappe emplacement under changed pressure and temperature conditions:

$$Cpx_1 + Opx + Pl_1 + H_2O + Ilm \rightarrow Amp + Pl_2 + Grt + Cpx_2 \pm Qz \pm Rt. \qquad \text{(R2)}$$

The least deformed parts of the Kågen gabbro exhibit some preserved assemblages (left hand side of ReactionR1) and some reacted products (right hand side of Reaction R1). The high strain regions at the margins represent the final assemblage in Reaction R2 (right hand side of R2). The low and mid strain areas show the progression of the mineral reaction R2 which is synchronous with deformation. There are remnants of clinopyroxene within some high strain amphibole layers; they represent former clinopyroxene grains that were not fully consumed in the amphibole producing reaction.

Mineral segregations show a heterogeneous distribution of reaction products, this relationship can occur through dissolution-reprecipitation (Robin 1979), poly-phase GBS (Hiraga *et al.* 2013) and nucleation of reaction products at microstructural or crystallographic sites associated with the reactant (Moore *et al.* 2015). In this study, thermodynamic modelling combined with conventional thermo-barometry show that reaction R2 took place at 690 ± 25 °C and 1.05 ± 0.15 GPa (within the uncertainties of the methods; Figure 8), which overlaps previously established P-T conditions for the solid state cooling of the gabbro (650-900°C, 0.7-0.9 GPa; Getsinger *et al.* 2013). Amphibole-plagioclase pairs show similar P-T conditions for the low, mid and high strain zones (Figure 8 inset, Table S1). Such a result indicates that the progression of mineral reactions were directly dependent on changes in H_2O content in the bulk rock rather than a change in P-T conditions during deformation (Finch *et al.* 2016, Giuntoli *et al.* 2018, Whyte *et al.* 2021).

Generally, in mid strain areas, the clinopyroxene is elongated and partially overgrown (Figure 4f bottom) or completely replaced (Figure 4f top) by elongated amphibole. However, in some areas the amphibole rims are absent and the clinopyroxene is mantled by garnet and occasional ilmenite (Figure 4d-e). The absence of amphibole, a hydrated mineral, in these regions indicates a limited aqueous fluid. These observed microstructural differences together with the presence of corona structures demonstrate that local equilibrium has prevailed, most likely because fluid availability in the gabbro is extremely localised, and therefore reaction R2 is incomplete in the fluid-deficient parts. In those parts where reaction R2 is complete, as is the case for the high strain zones, aqueous fluids must have been more abundant, and therefore we suggest the high strain zones (which have formed after the low and mid strain zones) had formed fluid pathways. It is unlikely that these pathways have exploited pre-existing features in the gabbro (e.g. Mancktelow & Pennacchioni 2005, Pennacchioni & Mancktelow 2018, Ceccato *et al.* 2020), because such features have been interpreted as mineralised veins leading to a different type of shear zones described by Getsinger *et al.* (2013). Essentially, the gabbro deformation was facilitated by mineral reactions, which in turn are facilitated by fluid transport and availability, i.e. an in-situ interaction of deformation and reaction (Rutter & Brodie 1985, Fitz Gerald & Stünitz 1993, Stünitz & Fitz Gerald 1993).

The change in chemistry of new (cpx$_2$) vs. magmatic (cpx$_1$) clinopyroxene grains and the change in amphibole (amp$_{A\text{-}D}$) chemistry when it neighbours different minerals (e.g. clinopyroxene, plagioclase or garnet), demonstrates that metamorphic reactions accompanied deformation (Figure 6, 7). New cpx$_2$ grains have a different chemical composition from that of the cpx$_1$ porphyroclasts, indicating homogeneous nucleation.

Nucleation of new cpx_2 with a different chemistry is a response to the change in P-T conditions since gabbro emplacement. The cpx_1 becomes unstable as aqueous fluid infiltrates the gabbro and enhances reaction R2. One of the consequences of the reaction-enhanced deformation is strain localisation (e.g. Rutter & Brodie 1985, Mansard *et al.* 2020a, 2020b). The zoning of amp_{B1} grains shows that it grew during a synkinematic reaction (Figure 6d). The change in mineral chemistry within or between neighbouring grains demonstrates that there has been local equilibrium between phases, most likely due to local variations in fluid availability. Mineral chemistry variations in the low and mid strain zones are associated with microstructural deformation features indicating that the dominant driving potential for crystallization of clinopyroxene and amphibole has been (local) chemical equilibrium and not internal strain energy, i.e., dynamic recrystallization was not the dominant process for reconstituting the microstructures (e.g. Stünitz 1998, Okudaira *et al.* 2015, Giuntoli *et al.* 2018, Soret *et al.* 2019, Mansard *et al.* 2020a, 2020b).When the P-T conditions for the high strain areas Kågen gabbro margins (this study) and those of the more preserved inner parts of the gabbro (Getsinger *et al.* 2013) are considered in relationship to the surrounding Vaddas Nappe metasediments (Faber *et al.* 2019), the results from this study lie on a P-T path connecting them (Figure 12). This suggests the margins of the Kågen gabbro may record the conditions for early stages of Vaddas Nappe thrusting after the gabbro emplacement, which took place at 439±1 Ma (Faber et al. 2019). The deformation observed in this study is part of the same event as the deformation of the metasediments at the Vaddas-Kalak boundary (432±6 Ma, $^{206}Pb/^{238}U$ ages; Faber et al. 2019), and the timing of the deformation of the gabbro margins can be constrained as between ca. 440-432 Ma.

5.2 Formation of crystallographic preferred orientation (CPO)

During deformation and metamorphism of the Kågen gabbro, the clinopyroxene CPO weakened as it destabilised, whilst the amphibole fabric strengthened as it precipitated (Figure 9-10). $\mathrm{Amp_A}$ nucleation within $\mathrm{cpx_1}$ grains in the low and mid strain areas indicate that initially $\mathrm{amp_A}$ replaced $\mathrm{cpx_1}$ topotactically along cleavage planes (Figures 4a-b, 4e, 9a-b, 10c; e.g. Shannon & Rossi 1964, Handy & Stünitz 2002, McNamara *et al.* 2012, Moore *et al.* 2015). The initial topotactic replacement of $\mathrm{cpx_1}$ by $\mathrm{amp_A}$ resulted in a direct inheritance of the $\mathrm{cpx_1}$ CPO (Figure 10) and a smaller mean grain size in low strain areas (Figure 5a). A similar situation is inferred for the initial corona rims of amphibole on $\mathrm{cpx_1}$. Thus, regions B and C in Figure 10 show strong CPO maxima for amphibole that do not relate to the shear geometry but are instead orientated closely to that of the host clinopyroxene grain.

The amphibole fabric evolved to an orientated growth fabric that is parallel to the shear direction. The growth character of the fabric is shown by the SPO strength increasing from low to high strain areas (Figure 5 d-f). If we consider regions A and D in Figure 10 (including the amphibole rim and tail surrounding relict $\mathrm{cpx_1}$ grain(s) and new $\mathrm{cpx_2}$ grains); the poles to the (100) plane of amphibole becomes orientated subnormal to the shear direction, and the amphibole [001] axes orientated subparallel to the shear direction. These orientations do not correlate with the weaker clinopyroxene CPO's, particularly in region D (Figure 10), where the clinopyroxene ($\mathrm{cpx_2}$) CPO is very weak and does not show a distinct fabric. The morphology of the $\mathrm{cpx_2}$ grains in the recrystallized tail in region D is similar to that of dynamic recrystallization during crystal plastic deformation, but chemical analysis shows that these new cpx_2 grains are compositionally different to the original cpx_1 grains (Figure 7a) and must have formed by homogeneous nucleation due to a chemical driving potential. Therefore, we suggest the new cpx_2 grains have primarily formed during the chemical reaction when clinopyroxene adjusts its composition from cpx_1 to cpx_2. The reaction takes place alongside deformation (accommodated by dissolution-precipitation creep), progressively destroying the clinopyroxene CPO and account for the change in chemistry (e.g. Stünitz 1993, Okudaira *et al.* 2015, Marti *et al.* 2017, Stünitz *et al.* 2020, Mansard *et al.* 2020a).

Thus, during the subsequent deformation process where amphibole rims and tails develop around cpx_1 grains in the mid strain regions, amp_A started to nucleate on the cpx_1 outer boundaries with the same initial inherited clinopyroxene crystal orientation, but during consumption of the clinopyroxene by reaction, the precipitating amphibole developed a distinct fabric different from the clinopyroxene host-controlled one. The CPO of the amphibole is best interpreted as a growth-controlled fabric. Amphiboles typically are elongated in the c-axis (Deer *et al.* 1997), which is the fastest growth direction. As this [001] direction is aligned with the stretching direction, it is inferred that the amphibole fabric during deformation is a growth-fabric, as inferred by Giuntoli *et al.* (2018) and for omphacite by Stünitz *et al.* (2020).

Amphibole ($amp_{A,B}$) overgrows and precipitates rims and tails around cpx_1 porphyroclasts (Figure 4a-f, 6). The CPO for these tails is progressively less related and therefore less inherited from the clinopyroxene (Figure 10). The SPO strength for amphibole increases from low to high strain areas suggesting amphibole growth in the high strain areas is crystallographic orientation controlled (Figure 5e). In the high strain areas, the amphibole ($amp_{B\text{-}D}$) CPO exhibits a maxima of (100) poles and a weak girdle subnormal to the shear direction and a strong maxima in the [001] axes parallel to the shear direction (e.g. Figure 9). The presence of the girdle in (100) and a very strong SPO parallel to the shear direction suggests a component of rigid body rotation around [001] (Figure 5f, 9c).

It is common to observe naturally deformed amphibole with the (100) pole aligned subnormal to the shear plane and the [001] direction aligned subparallel to the shear direction (e.g. Berger & Stünitz 1996, Imo*n et al*. 2004, Díaz Aspiroz *et al.* 2007, Tatham *et al*. 2008, Llana-Fúnez & Brown 2012, Getsinger *et al*. 2013, Okudaira *et al*. 2015, Elyaszadeh *et al*. 2018, Soret *et al*. 2019). This fabric has been shown to occur under middle to upper amphibolite facies conditions (650-750°C, 0.6-1 GPa), and commonly shows that amphibole grains are reoriented or grow (sub)parallel to the shear direction (Ko & Jung 2015). The primary slip vector in amphibole is <001>, and a strong amphibole CPO with (100) plane subnormal to foliation and [001] axes parallel to lineation could suggest that (100)<001> easy slip system can be important in generating this type of CPO (Díaz Aspiroz *et al.* 2007). However, in the case of the Kågen gabbro there are no amphibole porphyroclasts, from which the amphibole is recrystallized, so dynamic recrystallization and thus a dislocation creep origin of the amphibole CPO can be excluded.

The amphibole CPO observed in the Kågen gabbro is similar to other natural examples, and as amphibole is only present in minor proportions (if at all) in the original gabbro (Getsinge*r et al*. 2013), we propose that the strong fabric forms during precipitation (homogeneous nucleation) of the amphibole (e.g. Berger & Stünitz 1996, Getsinger & Hirth 2014, Giuntoli *et al.* 2018). The weak girdle of (100) poles in the high strain domains indicate minor rigid body rotation occurred around the [001] axes. It has been suggested that such girdles are formed through cataclastic flow forming a fine-grained matrix produced by fracturing and comminution (Imon *et al.* 2004, Kanagawa *et al.* 2008, Kim & Jung 2019). Cataclastic flow is unlikely in these samples, because (a) the confining pressures of ~1GPa make frictional processes unlikely, and (b) the larger and uniform grain size in higher strain domains without evidence for fracturing (Figure 3c, 4c) do not indicate brittle processes. Instead, the rigid body rotation of amphibole grains in the Kågen gabbro is likely to have occurred via progressive rotation in a mechanically weaker plagioclase matrix, facilitated by solution transfer, precipitation and grain growth of the amphiboles as they increase in modal amount.

Plagioclase shows a decrease in the mean grain size from low to high strain areas (Figure 5a-c). The larger grain size in low strain areas is due to the preservation of original magmatic pl_1. As deformation of the gabbro progresses, the large original grains are replaced by neo-crystallized plagioclase of a more sodic composition (pl_2; Figure 7d). Unlike the plagioclase studied by Gardner *et al.* (2021) where dissolution-precipitation is identified as the dominant deformation mechanism for plagioclase in a greenschist metagabbro, Ca-plagioclase is preserved in this study. This variation is likely due to a lack of brittle fracturing in the plagioclase preventing complete albitisation. The neo-crystallization also results in a slight elongation of pl_2 grains parallel to the shear direction (Figure 5f). The CPO of new plagioclase is weak, especially in areas where fine plagioclase grain coexist with amphibole (Figure 11; Kruse & Stünitz, 1999; Lapworth *et al.,* 2002; Mehl & Hirth, 2008). In the low strain regions the weak CPO is controlled by large original grains and does not represent a characteristic fabric type of crystal plasticity (Figure 11a; e.g.

Getsinger & Hirth 2014). Figure 11c shows that the plagioclase grain size is smaller in the polyphase areas than the monophase band, suggesting that grain growth is limited in the mixed phase areas. Deformation by diffusion creep in the high strain areas is most likely accommodated by GBS that is localised in polyphase layers where phase mixing occurs between amphibole and plagioclase (Figure 11c, polyphase layer). The weak plagioclase CPO in the high strain areas indicates a lack of crystal plasticity and the dominant deformation mechanism is inferred to be dissolution-precipitation creep (Figure 11). Diffusion creep with GBS inhibits development of a CPO and destroys pre-existing CPO's (Elliott 1973). Unlike amphibole, there is not a strong crystallographic control on plagioclase grain shape during precipitation resulting in a lack of CPO (Getsinger & Hirth 2014). Dissolution-precipitation creep is further supported as the primary deformation mechanism active in plagioclase by plagioclase chemistry change from more anorthic in low strain areas to more albitic in high strain zones (Figures 6c, 7d, 11c).

Quartz and calcite occur as inclusions in clinopyroxene and garnet grains or interstitially. Quartz is the more common and is usually associated with amphibole and garnet zones. This indicates there was excess silica during the metamorphic reactions to allow quartz precipitation (Figures 6b-d, S2). The lack of CPO fabric in the quartz suggests crystal plastic deformation was not dominant during and post precipitation (Figure S6). Calcite is occurs interstitially with a cuspate shape in amphibole zones but more commonly around garnet grains (Figures 6b-c, S2). The cuspate calcite morphology and weak CPO fabric suggests it infilled pore space late or after in the deformation (Figure S6). We suggest that these minerals did not undergo any crystal plasticity and precipitated late in the deformation history with no crystallographic orientation controlled growth.

5.3 *Wider implications*

Deformation of the Kågen gabbro margins is hypothesised to be associated with emplacement of the Vaddas Nappe on a P-T path from 690°C and 1.05 GPa to 630°C and 1.3 GPa (Figure 12a; Fabe*r et al*. 2019). Crystal plastic deformation may be expected in plagioclase and clinopyroxene at such conditions (Mauler *et al.* 2000, Rybacki & Dresen 2004), however no evidence for dislocation creep processes is observed here. Instead, we observe a change in chemistry and stable phase assemblage between the low and high strain regions (Figure 12b). Fluid pathways within the gabbro allowed metamorphic reactions to proceed and consequently enhanced strain localisation (e.g. Rutter & Brodie 1985, Finch *et al.* 2016, Whyte *et al.* 2021). The fluid supply was limited or infiltration was not pervasive thus allowing preservation of the dry, low strain gabbro pods. During emplacement and deformation of the Vaddas Nappe, the high strain zones formed fluid pathways and a network of anastomosing shear zones that localised deformation and left the low strain areas as dry pods (Figure 2).

It is often assumed that new small grains in a deformed rock is the result of dynamic recrystallization (e.g. Tullis & Yund 1992, Stünitz *et al.* 2003), however we show that the new clinopyroxene and plagioclase grains have a different chemistry to the larger original grains (Figure 6, 7). This indicates dissolution-precipitation is responsible for the formation of the new grains rather than a crystal-plastic mechanism. In addition, dislocation creep is considered a fabric strengthening mechanism (e.g. strong CPO) whereas diffusion creep is fabric weakening (e.g. no CPO), but when dissolution-precipitation creep is accompanied by orientated growth, the resultant amphibole CPO is strong. Deformation experiments of plagioclase and pyroxene mixtures by Marti *et al.* (2017, 2018) and Mansard *et al.* (2020a, 2020b) showed that amphibole coronas on pyroxene were more elongated in the deformed samples. These results indicate that amphibole has accommodated displacement via dissolution-precipitation creep. As dissolution precipitation creep is a type of diffusion creep, stress exponents for this type of deformation are expected to be as low as those for diffusion creep, i.e. in the order of $n{\sim}1$.

The processes that control deformation in the Kågen gabbro (e.g. DPC, rigid body rotation and GBS) are similar to those described in the garnet-clinopyroxene amphibolites formed during subduction initiation (Soret *et al.* 2019). Dissolution-precipitation creep alongside amphibole-forming metamorphic reactions in the Kågen gabbro are driven by variations in water activity. Fluid pathways in the gabbro resulted in strain localisation that in turn controlled the rheology (e.g. Marti *et al.* 2017, 2018, Soret *et al.* 2019, Mansard *et al.* 2020a, 2020b). Thus the deformation processes observed in the Kågen gabbro represent common processes controlling the development of hydrated mafic rocks, regardless of the geological setting.

6. Conclusions

Deformation at the margins of the Kågen gabbro on a P-T path from 690°C ± 25 °C and pressures of 1.0 to 1.1 GPa provides a natural example of how dissolution precipitation creep facilitates the deformation of mafic rocks during concomitant mineral reactions.

The dissolution part of the process takes in the reactants while the precipitation takes place in the new stable product phases. The mechanical properties of mafic rocks during deformation coupled with reactions are substantially weaker than for an assemblage of pyroxene/amphibole and plagioclase without reactions. Through chemical and microstructural analysis we have shown that metamorphic reactions primarily occurred in a fluid-rich environment, which resulted in strain localisation into the hydrating parts of the rock and subsequent weakening as metamorphic reaction progressed. Despite the strong crystal fabric and CPO in amphibole grains, dislocation creep was not the dominant deformation mechanism, instead dissolution-precipitation creep involving both, diffusion-accommodated GBS and diffusive mass transfer, has facilitated the deformation. The CPO is produced by the fastest growth direction and rigid particle rotation, i.e. by shape-factors of the precipitating amphibole. When deformation and mineral reactions occur simultaneously, strong rocks can become mechanically weak, at least transiently. Processes like dissolution-precipitation creep allow the mafic rocks to deform viscously at lower temperatures and lower stresses than expected for dislocation creep of the original constituent phases (pyroxene, amphibole, and plagioclase). Low stress exponents are expected for such a deformation.

Acknowledgements

The authors thank Amanda Getsinger for sample collection, documentation, and sample cutting. We thank Jiří Konopásek for discussions and suggestions during early chemical analysis and data processing. We thank Nicolas Rividi (Sorbonne Université, Camparis laboratory, France) for analytical support at the microprobe. We thank Toru Takeshita for editorial handling and the constructive reviews by Alberto Ceccato and Francesco Giuntoli have improved the present version of the manuscript substantially. MB thanks CAPES-Diku Project number 88881.117872/2016-01.

Data Availability

EBSD data for maps A8B 2b, 4b, 8a and 9b are available to download as channel text files from https://doi.org/10.17632/xhd6gs3fyc.1.

7. References

Allison, I. & La Tour, T.E. (1977) Brittle Deforamtion of Hornblende in a Mylonite: a Direct Geometrical Analogoue of Ductile Deformation By Translation Gliding. *Can J Earth Sci*, **14**, 1953–1961. doi:10.1139/e77-166

Andersen, T.B., Austrheim, H., Sturt, B.A., Pedersen, S. & Kjaersrud, K. (1982) Rb-Sr whole rock ages from Mageroy, north Norwegian Caledonides. *Nor. Geol. Tidsskr.*, **62**, 79–85.

Babaie, H.A. & La Tour, T.E. (1994) Semibrittle and cataclastic deformation of hornblende-quartz rocks in a ductile shear zone. *Tectonophysics*, **229**, 19–30. doi:10.1016/0040-1951(94)90003-5

Bachmann, F., Hielscher, R. & Schaeben, H. (2010) Texture analysis with MTEX- Free and open source software toolbox. *Solid State Phenom.*, **160**, 63–68. doi:10.4028/www.scientific.net/SSP.160.63

Berger, A. & Stünitz, H. (1996) Deformation mechanisms and reaction of hornblende: Examples from the Bergell tonalite (Central Alps). *Tectonophysics*, **257**, 149–174. doi:10.1016/0040-1951(95)00125-5

Biermann, C. & Roermund, H.L.M. van. (1983) Defect structures in naturally deformed clinoamphiboles - a TEM study. *Tectonophysics*, **95**, 267–278.

Brodie, K.H. & Rutter, E.H. (1985) On the relationship between deformation and metamorphism, with special reference to the behavior of basic rocks. *Metamorph. React. Kinet. Textures, Deform.*, 138–179. doi:10.1007/978-1-4612-5066-1_6

Bunge, H. J.: Texture Analysis in Materials Sciences, Buttleworth, London, 1982.

Bystricky, M. & Mackwell, S. (2001) Creep of dry clinopyroxene aggregates with deformation in the dislocation creep. *J. Geophys. Res.*, **106**, 13443–13454.

Carter, N.L. & Ave'Lallemant, H.G. (1970) High temperature flow of dunite and peridotite. *Geol. Soc. Am. Bull.*, **81**, 2181–2202.

Ceccato, A., Goncalves, P. & Pennacchioni, G. (2020) Temperature, fluid content and rheology of localized ductile shear zones in subsolidus cooling plutons. *J. Metamorph. Geol.*, **38**, 881–903. doi:10.1111/jmg.12553

Connolly, J.A.D. (2009) The geodynamic equation of state: What and how. *Geochemistry, Geophys. Geosystems*, **10**. doi:10.1029/2009GC002540

Connolly, J.A.D. & Kerrick, D.M. (1987) An algorithm and computer program for calculating composition phase diagrams. *Calphad*, **11**, 1–55. doi:10.1016/0364-5916(87)90018-6

Corfu, F., Gasser, D. & Chew, D.M. (2014) New perspectives on the caledonides of scandinavia and related areas: Introduction. *Geol. Soc. Spec. Publ.*, **390**, 1–8. doi:10.1144/SP390.28

Corfu, F., Torsvik, T.H., Andersen, T.B., Ashwal, L.D., Ramsay, D.M. & Roberts, R.J. (2006) Early Silurian mafic-ultramafic and granitic plutonism in contemporaneous flysch, Magerøy, northern Norway: U-Pb ages and regional significance. *J. Geol. Soc. London.*, **163**, 291–301. doi:10.1144/0016-764905-014

Cumbest, R.J., Drury, M.R., Roermund, H.L.M. van & Simpson, C. (1989) Dynamic recrystallization and chemical evolution of clinoamphibole from Senja, Norway. *Contrib. to Mineral. Petrol.*, **101**, 339–349. doi:10.1007/BF00375318

Deer, W.A., Howie, R.A. & Zussman, J. (1997) Chain silicates. in *Rock-forming minerals*, pp. 143–278.

Díaz Aspiroz, M., Lloyd, G.E. & Fernández, C. (2007) Development of lattice preferred orientation in clinoamphiboles deformed under low-pressure metamorphic conditions. A SEM/EBSD study of metabasites from the Aracena metamorphic belt (SW Spain). *J. Struct. Geol.*, **29**, 629–645. doi:10.1016/j.jsg.2006.10.010

Dimanov, A., Dresen, G., Xiao, X. & Wirth, R. (1999) Grain boundary diffusion creep of synthetic anorthite aggregates: The effect of water. *J. Geophys. Res. Solid Earth*, **104**, 10483–10497. doi:10.1029/1998jb900113

Dimanov, Alexandre & Dresen, G. (2005) Rheology of synthetic anorthite-diopside aggregates: Implications for ductile shear zones. *J. Geophys. Res. Solid Earth*, **110**, 1–24. doi:10.1029/2004JB003431

Dimanov, Alexandre, Lavie, M.P., Dresen, G., Ingrin, J. & Jaoul, O. (2003) Creep of polycrystalline anorthite and diopside. *J. Geophys. Res. Solid Earth*, **108**. doi:10.1029/2002jb001815

Dimanov, Alexandre, Raphanel, J. & Dresen, G. (2011) Newtonian flow of heterogeneous synthetic gabbros at high strain: Grain sliding, ductile failure, and contrasting local mechanisms and interactions. *Eur. J. Mineral.*, **23**, 303–322. doi:10.1127/0935-1221/2011/0023-2110

Dollinger, G. & Blacic, J.D. (1975) Deformation mechanisms in experimentally and naturally deformed amphiboles. *Earth Planet. Sci. Lett.*, **26**, 409–416. doi:10.1016/0012-821X(75)90016-3

Drury, M.R. & Urai, J.L. (1990) Deformation-related recrystallization processes. *Tectonophysics*, **172**, 235–253. doi:10.1109/IMFEDK.2013.6602261

Elliott, D. (1973) Diffusion flow laws in metamorphic rocks. *Bull. Geol. Soc. Am.*, **84**, 2645–2664. doi:10.1130/0016-7606(1973)84<2645:DFLIMR>2.0.CO;2

Elyaszadeh, R., Prior, D.J., Sarkarinejad, K. & Mansouri, H. (2018) Different slip systems controlling crystallographic preferred orientation and intracrystalline deformation of amphibole in mylonites from the Neyriz mantle diapir, Iran. *J. Struct. Geol.*, **107**, 38–52, Elsevier. doi:10.1016/j.jsg.2017.11.020

Faber, C., Stünitz, H., Gasser, D., Jeřábek, P., Kraus, K., Corfu, F., Ravna, E.K., *et al.* (2019) Anticlockwise metamorphic pressure-Temperature paths and nappe stacking in the Reisa Nappe Complex in the Scandinavian Caledonides, northern Norway: Evidence for weakening of lower continental crust before and during continental collision. *Solid Earth*, **10**, 117–148. doi:10.5194/se-10-117-2019

Finch, M.A., Weinberg, R.F. & Hunter, N.J.R. (2016) Water loss and the origin of thick ultramylonites. *Geology*, **44**, 599–602. doi:10.1130/G37972.1

Fitz Gerald, J.D. & Stünitz, H. (1993) Deformation of granitoids at low metamorphic grade. I: Reactions and grain size reduction. *Tectonophysics*, **221**, 299–324.

Gardner, J., Wheeler, J. & Mariani, E. (2021) Lithos Interactions between deformation and dissolution-precipitation reactions in plagioclase feldspar at greenschist facies. *Lithos*, **396–397**, 106241, Elsevier B.V. doi:10.1016/j.lithos.2021.106241

Gasser, D., Jeřábek, P., Faber, C., Stünitz, H., Menegon, L., Corfu, F., Erambert, M., *et al.* (2015) Behaviour of geochronometers and timing of metamorphic reactions during deformation at lower crustal conditions: Phase equilibrium modelling and U-Pb dating of zircon, monazite, rutile and titanite from the Kalak Nappe Complex, northern Norway. *J. Metamorph. Geol.*, **33**, 513–534. doi:10.1111/jmg.12131

Getsinger, A.J. & Hirth, G. (2014) Amphibole fabric formation during diffusion creep and the rheology of shear zones. *Geology*, **42**, 535–538. doi:10.1130/G35327.1

Getsinger, A.J., Hirth, G., Stünitz, H. & Goergen, E.T. (2013) Influence of water on rheology and strain localization in the lower continental crust. *Geochemistry, Geophys. Geosystems*, **14**, 2247–2264. doi:10.1002/ggge.20148

Giuntoli, F., Menegon, L. & Warren, C.J. (2018) Replacement reactions and deformation by dissolution and precipitation processes in amphibolites. *J. Metamorph. Geol.*, **36**, 1263–1286. doi:10.1111/jmg.12445

Graziani, R., Larson, K.P. & Soret, M. (2020) The effect of hydrous mineral content on competitive strain localization mechanisms in felsic granulites. *J. Struct. Geol.*, **134**, 104015, Elsevier Ltd. doi:10.1016/j.jsg.2020.104015

Green, E.C.R., White, R.W., Diener, J.F.A., Powell, R., Holland, T. & Palin, R.M. (2016) Activity–composition relations for the calculation of partial melting equilibria in metabasic rocks. *J. Metamorph. Geol.*, **34**, 845–869. doi:10.1111/jmg.12211

Hacker, B.R. & Christie, J.M. (1990) Brittle/ductile and plastic/cataclastic transitions in experimentally deformed and metamorphosed amphibolite. *Geophys. Monogr.*, **56**, 127–147.

Handy, M.R. & Stünitz, H. (2002) Strain localization by fracturing and reaction weakening -A mechanism for initiating exhumation of subcontinental mantle beneath rifted margins. *Geol. Soc. Spec. Publ.*, **200**, 387–407. doi:10.1144/GSL.SP.2001.200.01.22

Hiraga, T., Miyazaki, T., Yoshida, H. & Zimmerman, M.E. (2013) Comparison of microstructures in superplastically deformed synthetic materials and natural mylonites: Mineral aggregation via grain boundary sliding. *Geology*, **41**, 959–962. doi:10.1130/G34407.1

Holland, T. & Blundy, J. (1994) Non-ideal interactions in calcic amphiboles and their bearing on amphibole-plagioclase thermometry. *Contrib. to Mineral. Petrol.*, **116**, 433–447. doi:10.1007/BF00310910

Holland, T. & Powell, R. (2003) Activity-compositions relations for phases in petrological calculations: An asymetric multicomponent formulation. *Contrib. to Mineral. Petrol.*, **145**, 492–501. doi:10.1007/s00410-003-0464-z

Holland, T. & Powell, R. (2011) An improved and extended internally consistent thermodynamic dataset for phases of petrological interest, involving a new equation of state for solids. *J. Metamorph. Geol.*, **29**, 333–383. doi:10.1111/j.1525-1314.2010.00923.x

Imon, R., Okudaira, T. & Fujimoto, A. (2002) Dissolution and precipitation processes in deformed amphibolites: An example from the ductile shear zone of the Ryoke metamorphic belt, SW Japan. *J. Metamorph. Geol.*, **20**, 297–308. doi:10.1046/j.1525-1314.2002.00367.x

Imon, R., Okudaira, T. & Kanagawa, K. (2004) Development of shape- and lattice-preferred orientations of amphibole grains during initial cataclastic deformation and subsequent deformation by dissolution-precipitation creep in amphibolites from the Ryoke metamorphic belt, SW Japan. *J. Struct. Geol.*, **26**, 793–805. doi:10.1016/j.jsg.2003.09.004

Jessell, M.W. (1987) Grain-boundary migration microstructures in a naturally deformed quartzite. *J. Struct. Geol.*, **9**, 1007–1014. doi:10.1016/0191-8141(87)90008-3

Ji, S., Shao, T., Michibayashi, K., Long, C., Wang, Q., Kondo, Y., Zhao, W., *et al.* (2013) A new calibration of seismic velocities, anisotropy, fabrics, and elastic moduli of amphibole-rich rocks. *J. Geophys. Res. E Planets*, **118**, 4699–4728. doi:10.1002/jgrb.50352

Kanagawa, K., Shimano, H. & Hiroi, Y. (2008) Mylonitic deformation of gabbro in the lower crust: A case study from the Pankenushi gabbro in the Hidaka metamorphic belt of central Hokkaido, Japan. *J. Struct. Biol.*, **30**, 1150–1166. doi:10.1016/j.jsg.2008.05.007

Kim, J. & Jung, H. (2019) New Crystal Preferred Orientation of Amphibole Experimentally Found in Simple Shear. *Geophys. Res. Lett.*, **46**, 12996–13005. doi:10.1029/2019GL085189

Ko, B. & Jung, H. (2015) Crystal preferred orientation of an amphibole experimentally deformed by simple shear. *Nat. Commun.*, **6**, Nature Publishing Group.

doi:10.1038/ncomms7586

Krogh, E.J. (1988) The garnet-clinopyroxene Fe-Mg geothermometer - a reinterpretation of existing experimental data. *Contrib. to Mineral. Petrol.*, **99**, 44–48. doi:10.1007/BF00399364

Kruse, R. & Stünitz, H. (1999) Deformation mechanisms and phase distribution in mafic high-temperature mylonites from the Jotun Nappe, southern Norway. *Tectonophysics*, **303**, 223–249. doi:10.1016/S0040-1951(98)00255-8

Kruse, R., Stünitz, H. & Kunze, K. (2001) Dynamic recrystallization processes in plagioclase porphyroclasts. *J. Struct. Geol.*, **23**, 1781–1802. doi:10.1016/S0191-8141(01)00030-X

Langdon, T.G. (2006) Grain boundary sliding revisited: Developments in sliding over four decades. *J. Mater. Sci.*, **41**, 597–609. doi:10.1007/s10853-006-6476-0

Lapworth, T., Wheeler, J. & Prior, D.J. (2002) The deformation of plagioclase investigated using electron backscatter diffraction crystallographic preferred orientation data. *J. Struct. Geol.*, **24**, 387–399. doi:10.1016/S0191-8141(01)00057-8

Leake, B.E., Woolley, A.R., Arps, C.E.S., Birch, W.D., Gilbert, M.C., Grice, J.D., Hawthorne, F.C., *et al.* (1997) Nomenclature of amphiboles: Report of the subcommittee on amphiboles of the international mineralogical association, commission on new minerals and mineral names. *Can. Mineral.*, **35**, 219–246.

Lindahl, I., Stevens, B.P.J. & Zwaan, K.B. (2005) The geology of the Váddás area, Troms: a key to our understanding of the Upper Allochthon in the Caledonides of northern

Norway. *Norges Geol. undersøkelse-Bulletin*, **445**, 5–43.

Llana-Fúnez, S. & Brown, D. (2012) Contribution of crystallographic preferred orientation to seismic anisotropy across a surface analog of the continental Moho at Cabo Ortegal, Spain. *Bull. Geol. Soc. Am.*, **124**, 1495–1513. doi:10.1130/B30568.1

Lloyd, G.E., Butler, R.W.H., Casey, M., Tatham, D.J. & Mainprice, D. (2011) Constraints on the seismic properties of the middle and lower continental crust. *Geol. Soc. Spec. Publ.*, **360**, 7–32. doi:10.1144/SP360.2

Mainprice, D. & Nicolas, A. (1989) Development of shape and lattice preferred orientations: application to the seismic anisotropy of the lower crust. *J. Struct. Geol.*, **11**, 175–189. doi:10.1016/0191-8141(89)90042-4

Mainprice, D., & Silver, P.G. (1993) Interpretation of SKS-waves using samples from the subcontinental lithosphere. *Physics of the Earth and Planetary Interiors*, **78**(3-4), 257-280. doi:10.1016/0031-9201(93)90160-B

Mancktelow, N.S. & Pennacchioni, G. (2005) The control of precursor brittle fracture and fluid-rock interaction on the development of single and paired ductile shear zones. *J. Struct. Geol.*, **27**, 645–661. doi:10.1016/j.jsg.2004.12.001

Mansard, N., Stünitz, H., Raimbourg, H. & Pr, J. (2020) The role of deformation-reaction interactions to localize strain in polymineralic rocks : Insights from experimentally deformed plagioclase-pyroxene assemblages, **134**. doi:10.1016/j.jsg.2020.104008

Mansard, N., Stünitz, H., Raimbourg, H., Précigout, J., Plunder, A. & Nègre, L. (2020) Relationship between microstructures and resistance in mafic assemblages that deform and transform. *Solid Earth*, **11**, 2141–2167. doi:10.5194/se-11-2141-2020

Marshall, D.B. & McLaren, A.C. (1977) Elastic twinning in experimentally deformed plagioclase feldspars. *Phys. Chem. Miner.*, **41**, 231–240. doi:10.1002/pssa.2210410128

Marti, S., Stünitz, H., Heilbronner, R., Plümper, O. & Drury, M. (2017) Experimental investigation of the brittle-viscous transition in mafic rocks – Interplay between fracturing , reaction , and viscous deformation. *J. Struct. Geol.*, **105**, 62–79, Elsevier. doi:10.1016/j.jsg.2017.10.011

Marti, S., Stünitz, H., Heilbronner, R., Plümper, O. & Kilian, R. (2018) Syn-kinematic hydration reactions, grain size reduction, and dissolution-precipitation creep in experimentally deformed plagioclase-pyroxene mixtures. *Solid Earth*, **9**, 985–1009. doi:10.5194/se-9-985-2018

Mauler, A., Bystricky, M., Kunze, K. & Mackwell, S. (2000) Microstructures and lattice preferred orientations in experimentally deformed clinopyroxene aggregates. *J. Struct. Geol.*, **22**, 1633–1648. doi:10.1016/S0191-8141(00)00073-0

McNamara, D.D., Wheeler, J., Pearce, M.A. & Prior, D.J. (2012) Fabrics produced mimetically during static metamorphism in retrogressed eclogites from the Zermatt-Saas zone, Western Italian Alps. *J. Struct. Geol.*, **44**, 167–178, Elsevier Ltd. doi:10.1016/j.jsg.2012.08.006

Mehl, L. & Hirth, G. (2008) Plagioclase preferred orientation in layered mylonites: Evaluation of flow laws for the lower crust. *J. Geophys. Res. Solid Earth*, **113**, 1–19. doi:10.1029/2007JB005075

Miranda, E.A., Hirth, G. & John, B.E. (2016) Microstructural evidence for the transition from dislocation creep to dislocation-accommodated grain boundary sliding in naturally deformed plagioclase. *J. Struct. Geol.*, **92**, 30–45, Elsevier Ltd. doi:10.1016/j.jsg.2016.09.002

Moghadam, H.S., Stern, R.J. & Rahgoshay, M. (2010) The Dehshir ophiolite (central Iran): Geochemical constraints on the origin and evolution of the inner Zagros ophiolite belt. *Bull. Geol. Soc. Am.*, **122**, 1516–1547. doi:10.1130/B30066.1

Molina, J.F., Moreno, J.A., Castro, A., Rodríguez, C. & Fershtater, G.B. (2015) Calcic amphibole thermobarometry in metamorphic and igneous rocks: New calibrations based on plagioclase/amphibole Al-Si partitioning and amphibole/liquid Mg partitioning. *Lithos*, **232**, 286–305, Elsevier B.V. doi:10.1016/j.lithos.2015.06.027

Moore, S.J., Cesare, B. & Carlson, W.D. (2015) Epitaxial nucleation of garnet on biotite in the polymetamorphic metapelites surrounding the Vedrette di Ries intrusion (Italian Eastern Alps). *Eur. J. Mineral.*, **27**, 5–18. doi:10.1127/ejm/2015/0027-2414

Morrison-Smith, D.J. (1976) Transmission electron microscopy of experimentally deformed hornblende. *Am. Mineral.*, **61**, 272–280. doi:10.1144/gsjgs.132.3.0343

Nyman, M.W., Law, R.D. & Smelik, E.A. (1992) Cataclastic deformation mechanism for the development of core-mantle structures in amphibole. *Geology*, **20**, 455–458. doi:10.1130/0091-7613(1992)020<0455:CDMFTD>2.3.CO;2

Okudaira, T., Jeřábek, P., Stünitz, H. & Fusseis, F. (2015) High-temperature fracturing and subsequent grain-size- sensitive creep in lower crustal gabbros: Evidence for coseismic loading followed by creep during decaying stress in the lower crust? *J.*

Geophys. Res. Solid Earth, **120**, 3119–3141. doi:doi:10.1002/ 2014JB011708

Pearce, M.A., Wheeler, J. & Prior, D.J. (2011) Relative strength of mafic and felsic rocks during amphibolite facies metamorphism and deformation. *J. Struct. Geol.*, **33**, 662–675, Elsevier Ltd. doi:10.1016/j.jsg.2011.01.002

Pennacchioni, G. & Mancktelow, N.S. (2018) Small-scale ductile shear zones: Neither extending, nor thickening, nor narrowing. *Earth-Science Rev.*, **184**, 1–12. doi:10.1016/j.earscirev.2018.06.004

Platt, J.P. & Behr, W.M. (2011) Grainsize evolution in ductile shear zones: Implications for strain localization and the strength of the lithosphere. *J. Struct. Geol.*, **33**, 537–550, Elsevier Ltd. doi:10.1016/j.jsg.2011.01.018

Poirier, J.P. (1985) *Creep of Crystals*, Cambridge University Press. doi:https://doi.org/10.1017/CBO9780511564451

Powell, R. (1985) Regression diagnostics and robust regression in geothermometer/geobarometer calibration: the garnet- clinopyroxene geothermometer revisited. *J. Metamorph. Geol.*, **3**, 231–243. doi:https://doi.org/10.1111/j.1525-1314.1985.tb00319.x

Roberts, D. & Sturt, B.A. (1980) Caledonian deformation in Norway. *J. Geol. Soc. London.*, **137**, 241–250. doi:10.1144/gsjgs.137.3.0241

Robin, P.Y.F. (1979) Theory of metamorphic segregation and related processes. *Geochim. Cosmochim. Acta*, **43**, 1587–1600. doi:10.1016/0016-7037(79)90179-0

Roermund, H.L.M. van & Lardeaux, J.M. (1991) Modification of antiphase domain sizes in omphacite by dislocation glide and creep mechanisms and its petrological consequences. *Mineral. Mag.*, **55**, 397–407. doi:10.1180/minmag.1991.055.380.09

Rooney, T.P., Riecker, R.E. & Gavasci, A.T. (1975) Hornblende deformation features. *Geology*, **3**, 364–366.

Rooney, T.P., Riecker, R.E. & Ross, M. (1970) Deformation Twins in Hornblende. *Science (80-.).*, **169**, 173–175. doi:10.1126/science.169.3941.173

Rudnick, R.L. & Fountain, D.M. (1995) Nature and composition of the continental crust: a lower crustal perspective. *Rev. Geophys.*, **33**, 267–309. doi:10.1029/95rg01302

Rutter, E.H. (1983) Pressure solution in nature, theory and experiment. *J. Geol. Soc. London.*, **140**, 725–740. doi:10.1144/gsjgs.140.5.0725

Rutter, E.H. & Brodie, K.H. (1985) The permeation of water into hydrating shear zones. in *Metamorphic Reactions: Kinetics, Textures, and Deformation*, pp. 242–250, Springe, New York, NY. doi:10.1007/978-1-4612-5066-1_9

Rybacki, E. & Dresen, G. (2004) Deformation mechanism maps for feldspar rocks. *Tectonophysics*, **382**, 173–187. doi:10.1016/j.tecto.2004.01.006

Shannon, R.D. & Rossi, R.C. (1964) Definition of Topotaxy. *Nature*, **202**, 1001–1003. doi:10.1038/2021001a0

Siegesmund, S., Helming, K. & Kruse, R. (1994) Complete texture analysis of a deformed amphibolite: comparison between neutron diffraction and U-stage data. *J. Struct. Geol.*, **16**, 131–142. doi:10.1016/0191-8141(94)90024-8

Skemer, P., Katayama, I., Jiang, Z., & Karato, S. I. (2005) The misorientation index:

Development of a new method for calculating the strength of lattice-preferred orientation. *Tectonophysics*, **411**(1-4), 157-167. doi:10.1016/j.tecto.2005.08.023

Skrotzki, W. (1992) Defect structure and deformation mechanisms in naturally deformed hornblende. *Phys. Status Solidi*, **131**, 605–624. doi:10.1002/pssa.2211310232

Soret, M., Agard, P., Ildefonse, B., Dubacq, B., Prigent, C. & Rosenberg, C. (2019) Deformation mechanisms in mafic amphibolites and granulites: record from the Semail metamorphic sole during subduction infancy. *Solid Earth Discuss.*, 1–36. doi:10.5194/se-2019-28

Stünitz, H., Fitz Gerald, J.D. & Tullis, J. (2003) Dislocation generation, slip systems, and dynamic recrystallization in experimentally deformed plagioclase single crystals. *Tectonophysics*, **372**, 215–233. doi:10.1016/S0040-1951(03)00241-5

Stünitz, H. (1993) Transition from fracturing to viscous flow in a naturally deformed metagabbro. in *Defects and processes in the solid state: geoscience applications-the MacLaren volume*, pp. 121–150.

Stünitz, H. (1998) Syndeformational recrystallization - dynamic or compositionally induced? *Contrib. to Mineral. Petrol.*, **131**, 219–236.

Stünitz, H. & Fitz Gerald, J.D. (1993) Deformation of granitoids at low metamorphic grade. II: Granular flow in albite-rich mylonites. *Tectonophysics*, **221**, 299–324. doi:10.1016/0040-1951(93)90164-F

Stünitz, H., Neufeld, K., Heilbronner, R., Finstad, A.K., Konopásek, J. & Mackenzie, J.R. (2020) Transformation weakening: Diffusion creep in eclogites as a result of interaction of mineral reactions and deformation. *J. Struct. Geol.*, **139**. doi:10.1016/j.jsg.2020.104129

Tatham, D.J., Lloyd, G.E., Butler, R.W.H. & Casey, M. (2008) Amphibole and lower crustal seismic properties. *Earth Planet. Sci. Lett.*, **267**, 118–128. doi:10.1016/j.epsl.2007.11.042

Terry, M.P. & Heidelbach, F. (2006) Deformation-enhanced metamorphic reactions and the rheology of high-pressure shear zones, Western Gneiss Region, Norway. *J. Metamorph. Geol.*, **24**, 3–18. doi:10.1111/j.1525-1314.2005.00618.x

Tullis, J. (1983) Deformation of feldspars. in *Feldspar mineralogy*, pp. 297–323.

Tullis, J. & Yund, R.A. (1992) The Brittle-Ductile Transition in Feldspar Aggregates: An Experimental Study. *Int. Geophys.*, **51**, 89–117. doi:10.1016/S0074-6142(08)62816-8

Wheeler, J. (1992) Importance of pressure solution and coble creep in the deformation of polymineralic rocks. *J. Geophys. Res. Solid Earth*, **97**, 4579–4586. doi:10.1029/91JB02476

White, R.W., Powell, R., Holland, T., Johnson, T.E. & Green, E.C.R. (2014) New mineral activity-composition relations for thermodynamic calculations in metapelitic systems. *J. Metamorph. Geol.*, **32**, 261–286. doi:10.1111/jmg.12071

Whitney, D.L. & Evans, B.W. (2010) Abbreviations for names of rock-forming minerals. *Am. Mineral.*, **95**, 185–187. doi:10.2138/am.2010.3371

Whyte, A.J., Weller, O.M., Copley, A.C. & St-Onge, M.R. (2021) Quantifying Water Diffusivity and Metamorphic Reaction Rates Within Mountain Belts, and Their

Implications for the Rheology of Cratons. *Geochemistry, Geophys. Geosystems*, **22**, 1–24. doi:10.1029/2021gc009988

Tables

Table 1: Summary of strain domains present in each thin section. Dominant strain domain present in EBSD maps is shown below the relevant host thin section.

Thin Section	**Strain domain present**		
EBSD map	Low	Mid	High
A8B1	**Y**		
1a	Y		
1b	Y		
A8B2	**Y**		
2a	Y		
2b	Y		
A8B3	**Y**	**Y**	**Y**
3a	Y		
3b			Y
3c		Y	
3d			Y
A8B4	**Y**	**Y**	**Y**
4a		Y	
4b		Y	
4c			Y
A8B5		**Y**	**Y**
5a		Y	
5b		Y	
A8B6	**Y**	**Y**	**Y**
6a		Y	
A8B7			**Y**
7a			Y
7b			Y
A8B8			**Y**
8a			Y
A8B9			**Y**
9a			Y
9b			Y
A8B10	**Y**		
10a	Y		
10b	Y		

Table 2: Selected representative analyses of garnet, clinopyroxene, plagioclase and amphibole from point analysis.

Min.	Grt	Grt	Grt	Cpx	Cpx	Cpx	Cpx	Pl	Pl	Pl	Pl	Pl	Amp	Amp	Amp	Amp
Thin section	A8b4	A8b4	A8b9	A8b1	A8b1	A8b4	A8b4	A8b1	A8b1	A8b4	A8b9	A8b9	A8b1	A8b4	A8b4	A8b9
Anal.	256/1	111/1	125/6	15/1	87 /1	224/1	92/1	101/8	61 /1	212/1	44 /1	12 /1	60/1	211/1	364/1	119/1
SiO_2	38.15	38.33	38.18	53.94	53.22	53.77	52.45	54.46	58.2	59.24	59.9	62.12	42.1	43.79	52.47	43.34
TiO_2	0.06	0.01	0.06	0.11	0.13	0.10	0.06	0.00	0.00	0.00	0.00	0.00	1.23	1.48	0.34	1.18
Al_2O_3	21.24	20.82	21.06	1.12	1.39	1.18	1.06	29.55	27.36	25.88	25.30	23.83	16.47	13.53	5.48	12.77
FeO	25.01	24.31	25.22	7.13	8.64	6.78	11.22	0.00	0.00	0.00	0.00	0.00	12.85	13.20	9.45	15.37
MnO	1.50	0.95	2.34	0.14	0.25	0.12	0.06	0.00	0.00	0.00	0.00	0.00	0.20	0.04	0.14	0.19
MgO	4.70	2.76	3.50	13.87	13.12	13.95	12.07	0.00	0.00	0.00	0.00	0.00	10.00	11.05	16.49	10.37
CaO	9.28	13.37	9.78	23.39	23.08	23.81	22.37	11.33	8.76	7.68	7.03	5.24	11.49	11.59	11.80	11.07
Na_2O	0.02	0.01	0.00	0.51	0.52	0.57	0.62	5.07	6.50	7.36	7.47	8.51	2.26	2.13	0.81	1.91
K_2O	0.00	0.00	0.04	0.00	0.00	0.00	0.00	0.00	0.05	0.07	0.09	0.06	0.46	0.43	0.09	0.46
Σ	100.0	100.5	100.2	100.2	100.4	100.3	99.9	100.4	100.8	100.2	100.0	99.8	97.1	97.2	97.1	96.7
Ox.	12	12	12	6	6	6	6	8	8	8	8	8	23	23	23	23
Si	2.99	3.01	3.01	1.99	1.98	1.99	1.98	2.44	2.58	2.64	2.67	2.75	6.20	6.44	7.43	6.42
Ti	0.00	0.00	0.00	0.00	0.00	0.00	0.00	0.00	0.00	0.00	0.00	0.00	2.86	2.35	0.91	2.23
Al	1.96	1.92	1.95	0.05	0.06	0.05	0.05	1.56	1.42	1.36	1.33	1.25	0.14	0.16	0.04	0.13
Fe_{tot}	1.64	1.59	1.66	0.22	0.27	0.21	0.35	0.00	0.00	0.00	0.00	0.00	1.58	1.62	1.12	1.90
Mn	0.10	0.06	0.16	0.00	0.01	0.00	0.00	0.00	0.00	0.00	0.00	0.00	0.02	0.01	0.02	0.02
Mg	0.55	0.32	0.41	0.76	0.73	0.77	0.68	0.00	0.00	0.00	0.00	0.00	2.20	2.42	3.48	2.29
Ca	0.78	1.12	0.82	0.93	0.92	0.94	0.91	0.55	0.42	0.37	0.36	0.25	1.81	1.83	1.79	1.76
Na	0.00	0.00	0.00	0.04	0.04	0.04	0.05	0.44	0.56	0.63	0.64	0.73	0.65	0.61	0.22	0.55
K	0.00	0.00	0.00	0.00	0.00	0.00	0.00	0.00	0.00	0.00	0.00	0.00	0.09	0.08	0.02	0.09
Prp	0.18	0.10	0.13	–	–	–	–	–	–	–	–	–	–	–	–	–
Alm	0.53	0.51	0.54	–	–	–	–	–	–	–	–	–	–	–	–	–
Grs	0.25	0.36	0.27	–	–	–	–	–	–	–	–	–	–	–	–	–
Sps	0.03	0.02	0.05	–	–	–	–	–	–	–	–	–	–	–	–	–
Mg#	0.25	0.17	0.20	0.78	0.73	0.79	0.66	–	–	–	–	–	0.58	0.60	0.76	0.55
An#	–	–	–	–	–	–	–	0.56	0.43	0.37	0.36	0.26	–	–	–	–

Abbreviations after Whitney and Evans (2010).

Figures

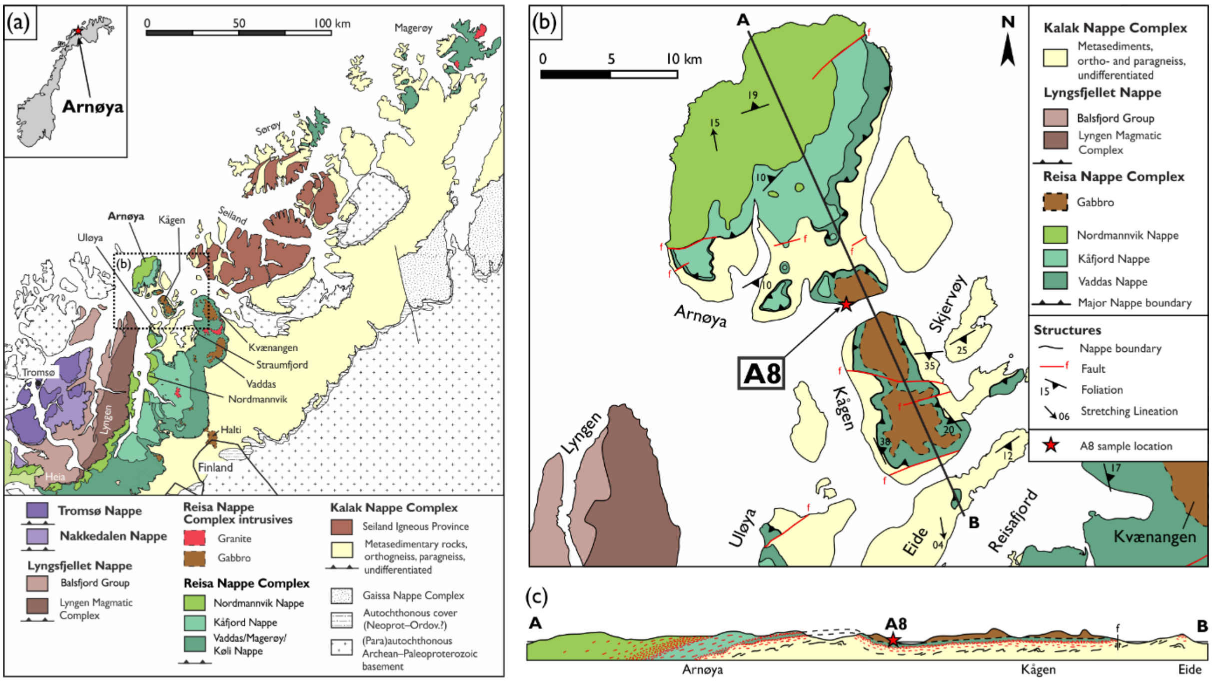

Figure 1: Geological map of the study area in Northern Norway. (a) North Norwegian Caledonides focussing on the Tromsø to Kalak Nappe Complexes. (b) Detailed map of Arnøya and Kågen to highlight the sample area in the Kågen gabbro. (c) Cross section through Arnøya and Kågen showing the gabbro intruded into the Vaddas Nappe. The density of red lines corresponds to the intensity of ductile deformation within and along boundaries between individual nappes. Caledonian foliations are shown in red, whereas black ones are possibly pre-date Caledonian deformation. After Faber et al. (2019).

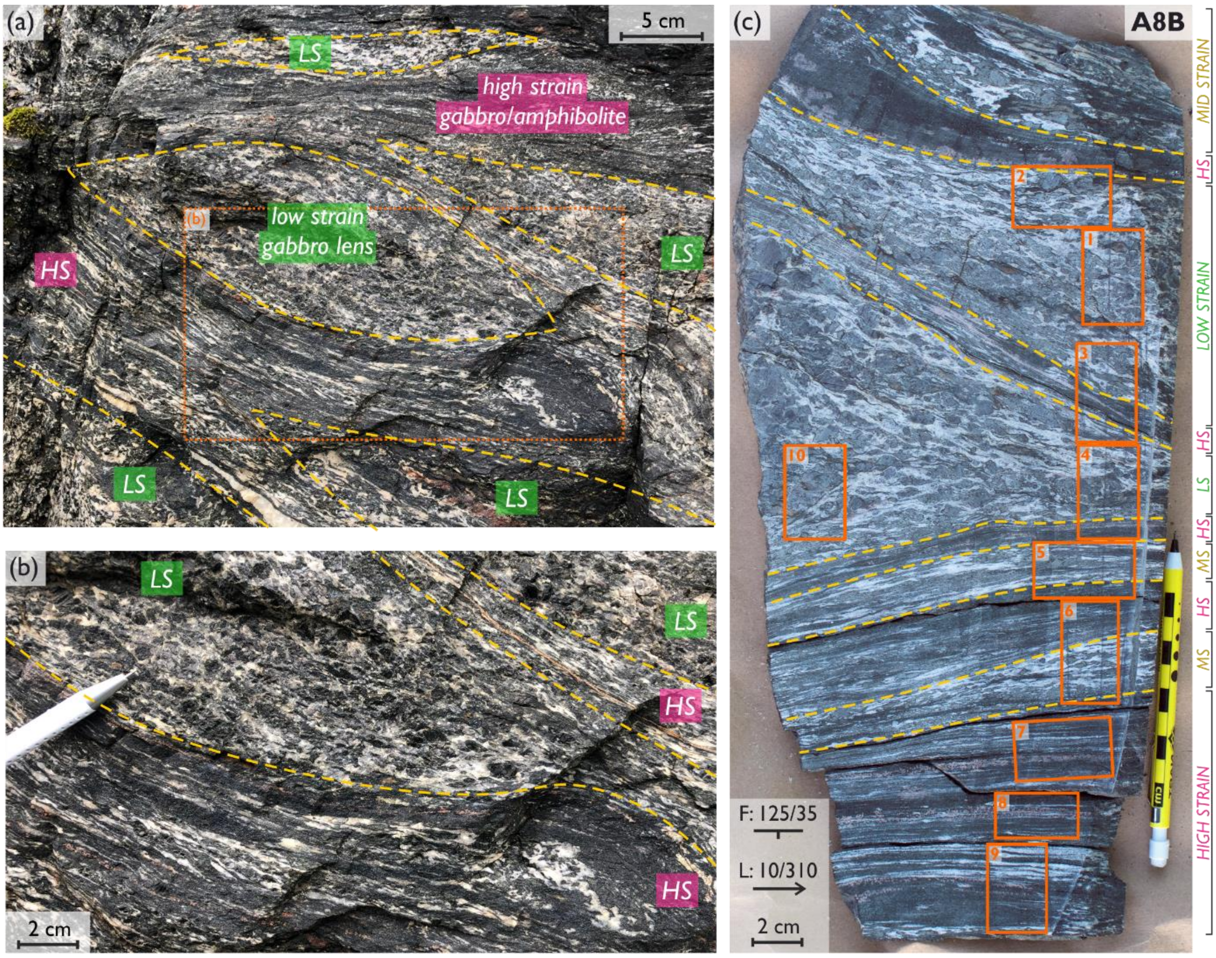

Figure 2: (a) Outcrop photograph of sample area (GPS: 70.04387°N, 20.71438°E), boundaries between low and high deformation areas highlighted by yellow dashed lines. (b) Detailed photograph from (a) with deformation boundaries and low/high strain zones identified. (c) Photograph of sample A8B with thin section locations highlighted by orange boxes, deformation boundaries between low, mid and high strain zones identified. LS, low strain; MS, mid strain; HS, high strain.

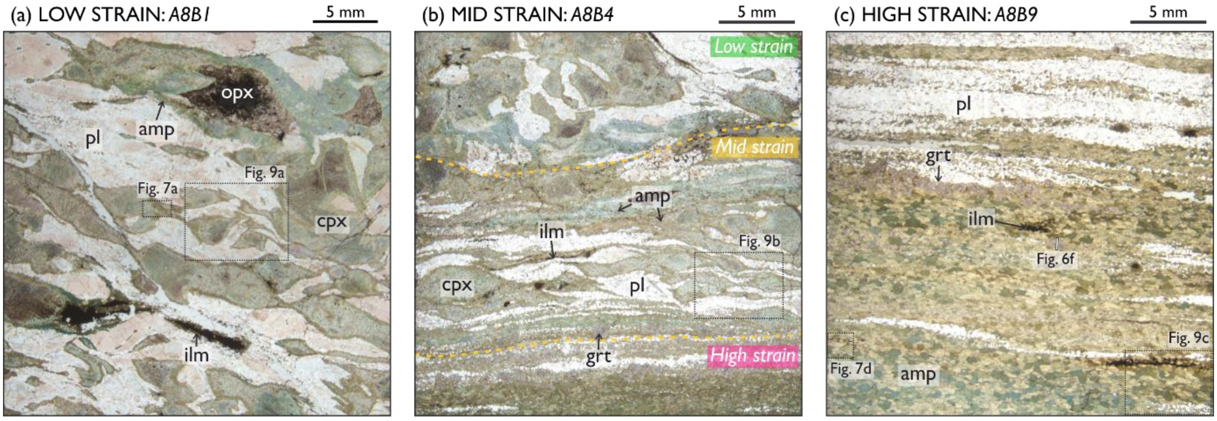

Figure 3: Overview thin section photomicrographs of representative (a) low, (b) mid and (c) high strain areas in sample A8B. (a) The low strain area shows clinopyroxene grains surrounded by amphibole coronas. Areas of chemical analysis (Fig. 7a) and EBSD (Fig. 9a) are indicated. (b) A characteristic mid strain area bound to the top by a low strain zone, and below by a high strain domain. Amphibole replacement of clinopyroxene is more extensive and plagioclase is highly recrystallized. Box Fig. 9b indicates area of EBSD analysis. (c) High strain region with amphibole and plagioclase layers. Garnet profile for Fig. 6f and EBSD map area for Fig. 9c are indicated.

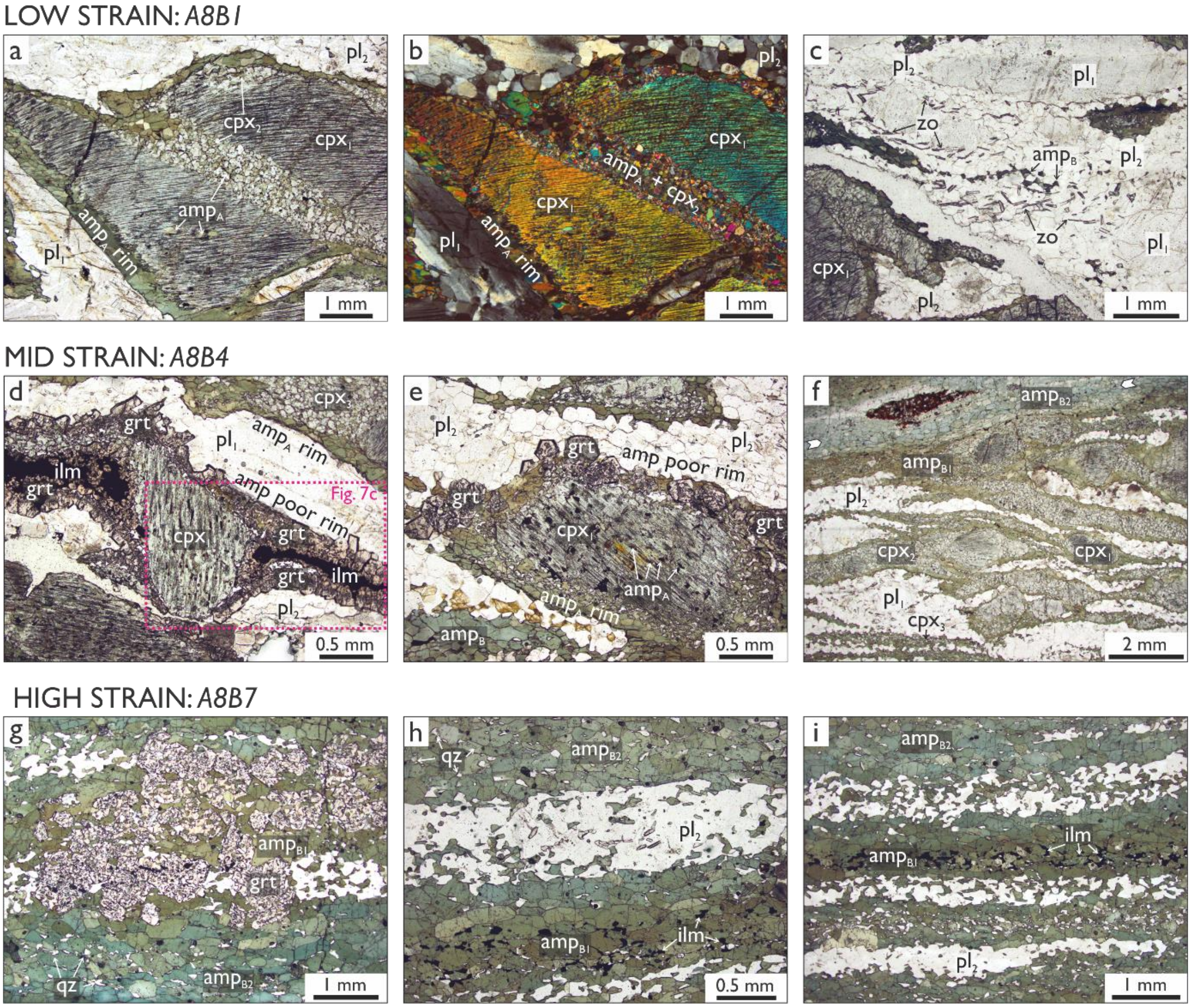

Figure 4: Detailed thin section photomicrographs of specific textures in (a-c) low, (d-f) mid and (g-i) high strain areas in sample A8B. Low strain: (a-b) clinopyroxene grain with recrystallized fracture and amphibole rim; (c) zoisite and isolated amphibole grains with pl$_1$ and pl$_2$ plagioclase grains. Mid strain: (d) cpx1 grain with garnet rim, rim reaction is amphibole poor; (e) clinopyroxene grain with garnet rim on the top and amphibole rim below; (f) amphibole replacement of clinopyroxene, top section between arrows shows complete amphibole replacement, below this original clinopyroxene grains are still preserved. High strain: (g) garnet within amphibole zone; (h-i) amphibole-plagioclase layers, amphibole is olive green coloured when associated with ilmenite (amp$_{B1}$) and otherwise jade green coloured (amp$_{B2}$). All photomicrographs are in plane polarised light except (b) that is under cross-polarised light.

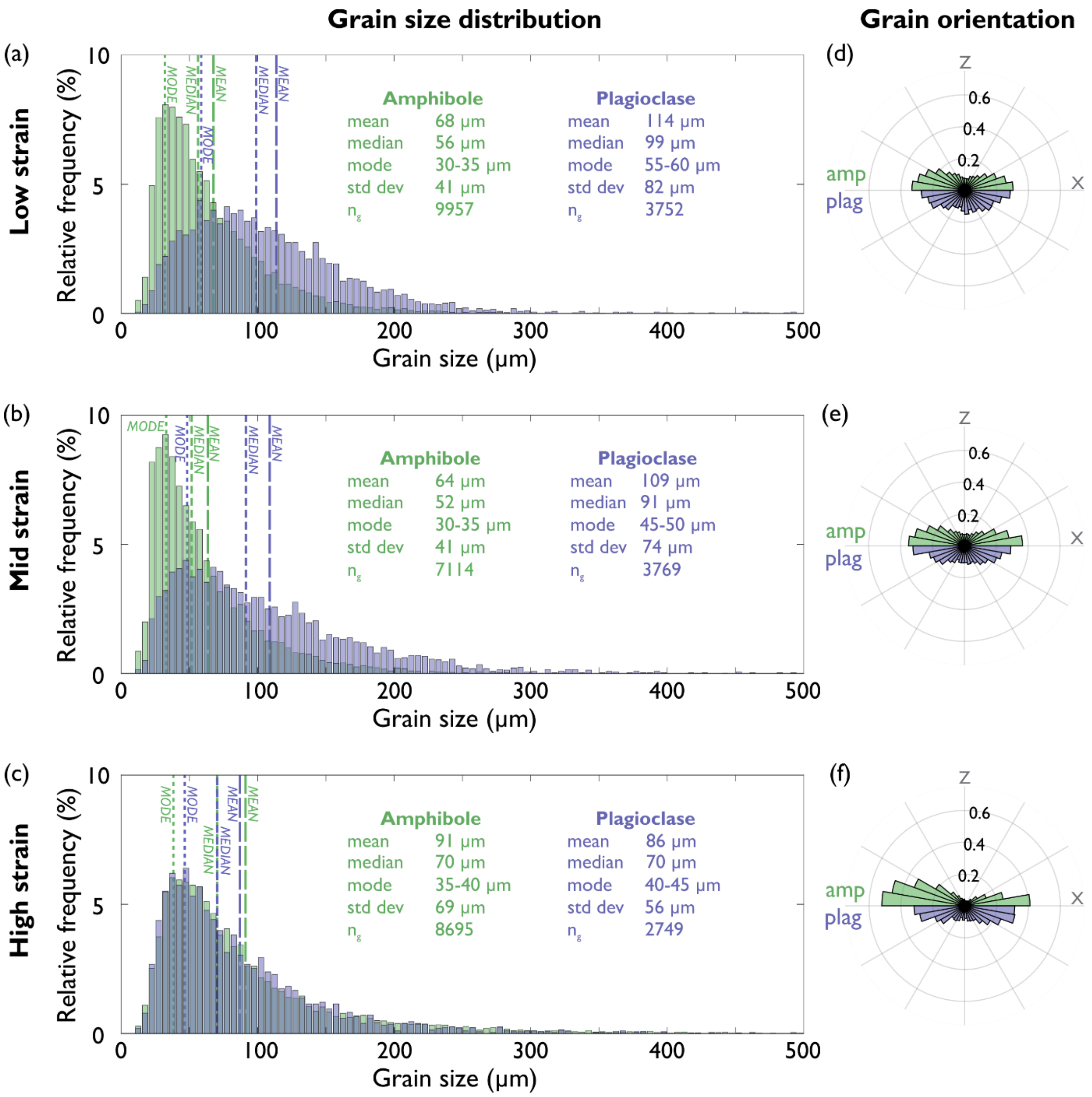

Figure 5: Grain size and shape properties for amphibole and plagioclase grains. (a-c) Grain size distribution with grain statistics for amphibole and plagioclase grains in low to high strain areas of the sample. (d-f) Normalised grain orientation or shape preferred orientation of amphibole and plagioclase grains in low to high strain areas. Grain data for each strain area is grouped together, low strain data includes data from EBSD maps 1a, 1b, 2a, 2b, 3a, 10a and 10b; mid strain data includes EBSD maps from 3c, 4b, 4c, 5a, 5b and 6a; and high strain data includes EBSD maps from 3b, 3d, 4a, 7a, 7b, 8a, 9a and 9b. Number of grains considered for each strain area is indicated by n_g. The frequency for rose diagrams is 0-1 and grain orientation is in the kinematic reference frame (the same as CPO pole figures in Figures 9-11).

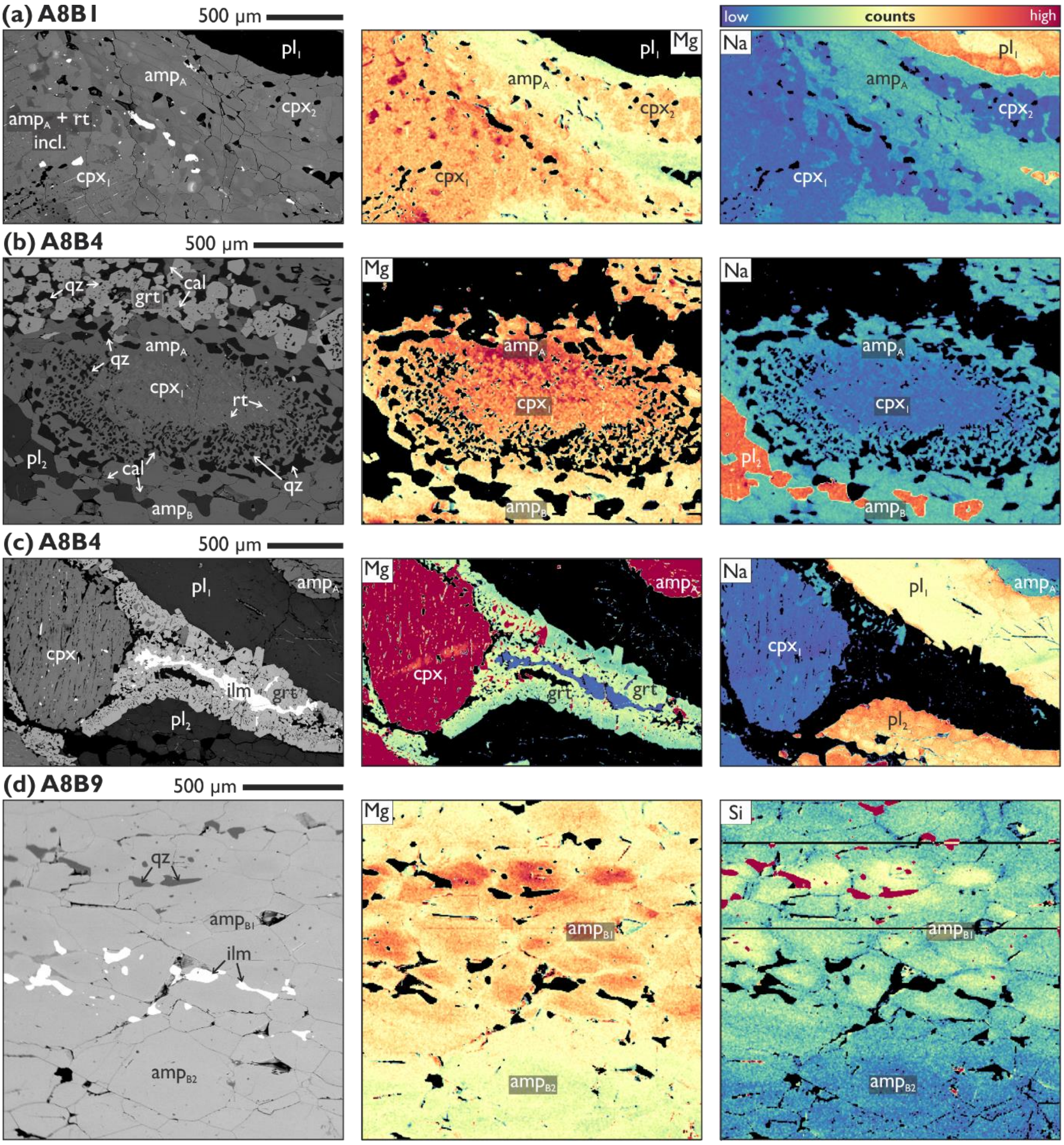

Figure 6: BSE images and compositional maps of detailed microstructural features in (a) low, (b-c) mid and (d) high strain areas of the Kågen gabbro margins. (a) Edge of clinopyroxene grain from Figure 3a, Mg and Na chemical maps highlight variations in clinopyroxene, amphibole and plagioclase chemistry. New small grains surrounding or forming tails around magmatic porphyroclasts have lower Mg and higher Na value than the original clinopyroxene grain (b) Clinopyroxene grain with amphibole replacement and garnet band, Mg map highlights variations in clinopyroxene and amphibole chemistry associated neighbour grains. (c) Amphibole-poor clinopyroxene grain from Figure 4d. Mg map highlights the variation in garnet chemistry when adjacent to plagioclase (low) or clinopyroxene/ilmenite (high). Plagioclase shows elevated Na when adjacent to garnet or amphibole as opposed to the core of pl_1 grains. New pl_2 grains are also have a higher Na. (d) Amphibole band in a high strain region. Mg- and Si-rich cores in amp_{B1} (olive green coloured) compared to amp_{B2} (jade green coloured).

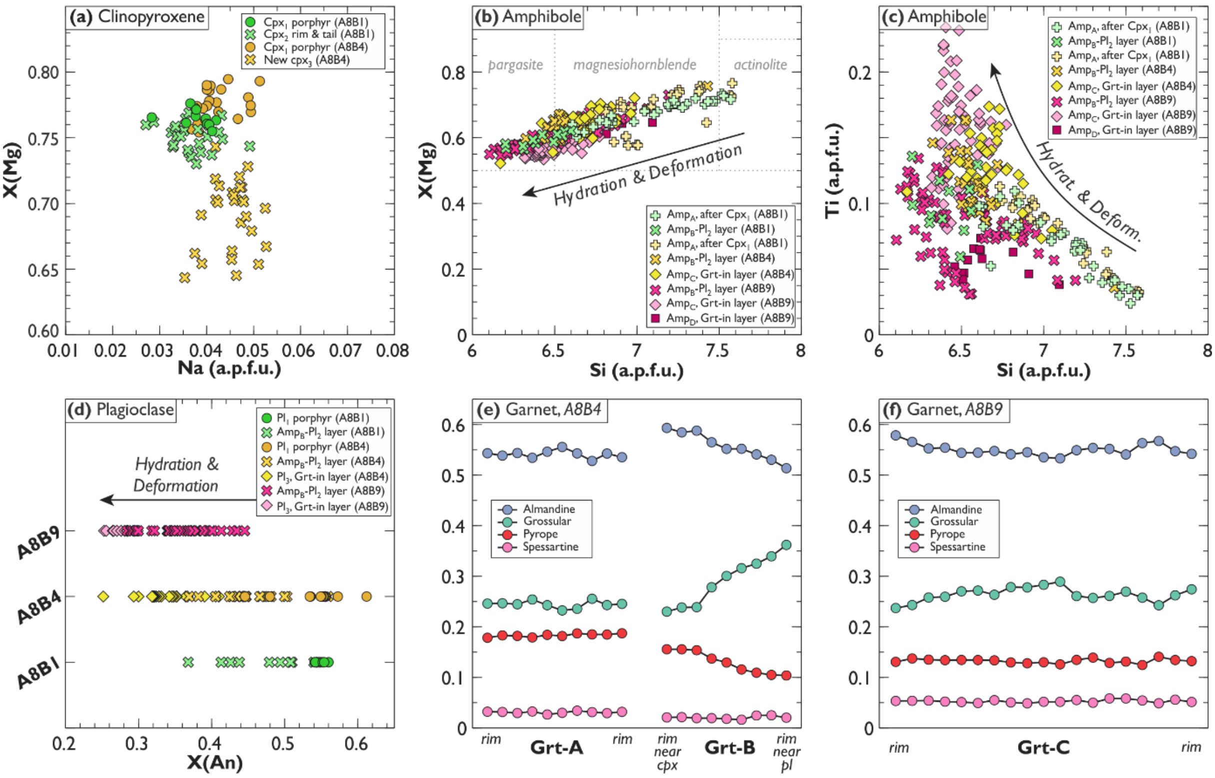

Figure 7: Point analyses and compositions for (a) clinopyroxene, (b-c) amphibole, (d) plagioclase and (e-f) garnet from low (A8B1), mid (A8B4) and high (A8B9) high strain areas of the Kågen gabbro margins.

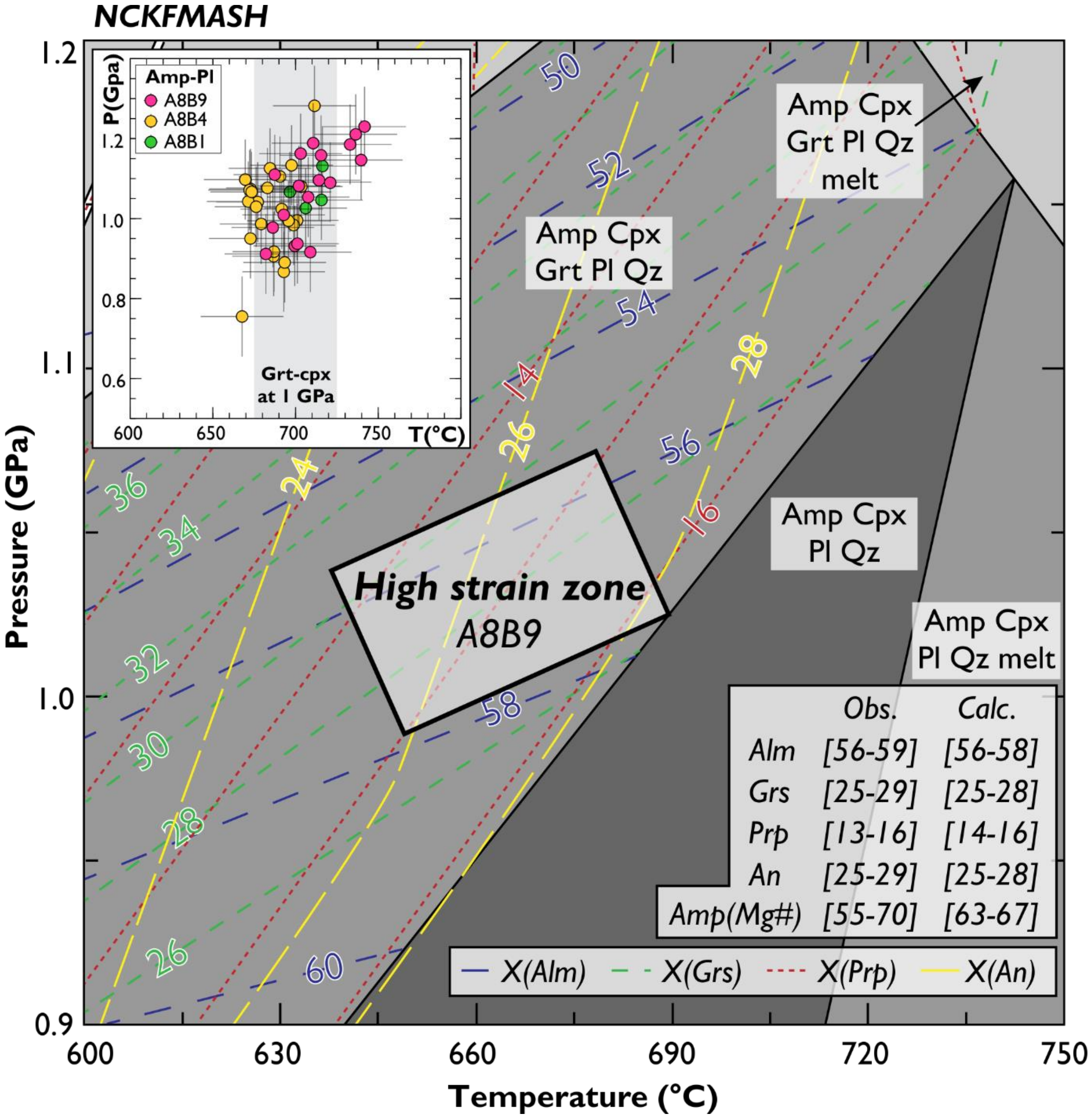

Figure 8: Estimated P-T conditions for the high strain areas of the Kågen gabbro margins. Isopleths represent end-member garnet and anorthite compositions. P-T conditions for high strain areas of the sample are in the highlighted box, observed and calculate compositions for garnet end-members (Alm, Grs, Prp), anorthite content (An) and amphibole (Amp) are shown in the bottom right. Oxide totals for pseudosection calculation are from a XRF measurements of a high strain area: Na_2O 2.88, MgO 8.27, Al_2O_3 14.11, SiO_2 49.97, CaO 11.49, FeO 8.54, H_2O 1.15. Inset shows amphibole-plagioclase thermobarometry for low, mid and high strain areas.

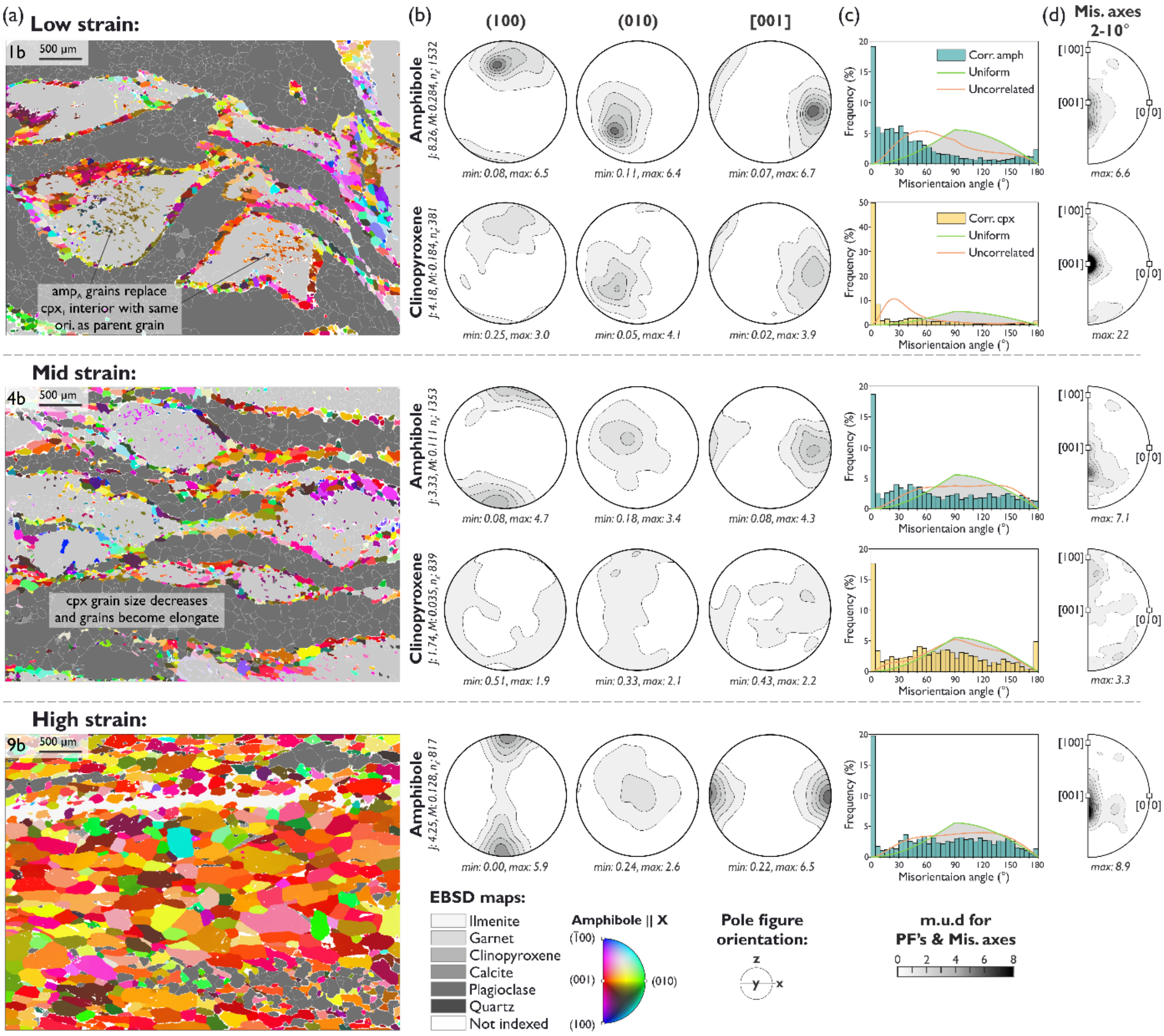

Figure 9: (a) EBSD maps of amphibole orientations coloured parallel to the X direction, all other minerals are shown in grey. All maps are at the same scale to highlight the change in grain size and texture between the differently deformed areas. (b) Pole figures showing amphibole CPO for the low to high strain areas, and clinopyroxene CPO for the low and mid strain areas. Clinopyroxene CPO's are not plotted for the high strain area as there is less than 1% present in the map giving skewed results due to lack of grains. All pole figures are equal area, lower hemisphere projections plotted as point per grain. J-index (e.g. Bunge 1982, Mainprice and Silver, 1993), M-index (Skemer et al. 2005) and number of grains (n_g) is shown for each set of pole figures. (c) Distribution of misorientation angles between correlated (adjacent) pixels (histogram) and between uncorrelated pixels (orange curve) of amphibole. The uniform (green) curve corresponds to the theoretical misorientation distribution for perfectly randomly oriented crystals. (d) Amphibole and clinopyroxene inverse pole figures showing the distribution of correlated misorientation axes (between 2 and 10°). All contours are multiples of uniform distribution (m.u.d).

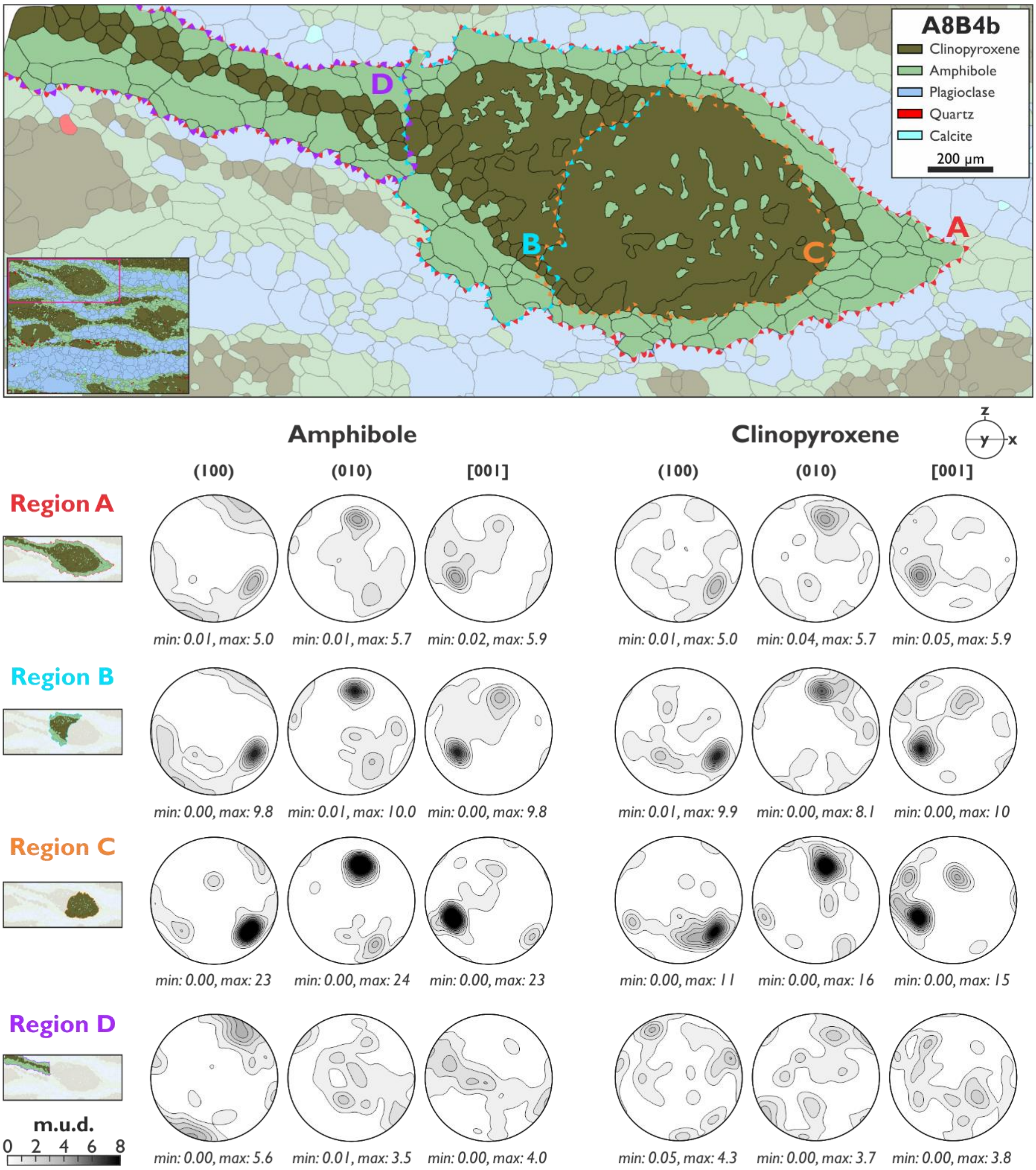

Figure 10: EBSD phase map of a clinopyroxene grain with amphibole corona, below are CPO pole figures for selected regions associated with the clinopyroxene grain. Region A (red) includes the clinopyroxene and all grains that mantle it. Region B (blue) contains the recrystallized portion of the clinopyroxene grain and the amphibole grains that mantle and are included in the clinopyroxene grain. Region C (orange) focusses on the right hand side of the clinopyroxene grain and the amphibole inclusions within the grain. Region D (purple) includes the clinopyroxene and amphibole grains in the recrystallized tail. All pole figures are equal area, lower hemisphere projections plotted as point per grain.

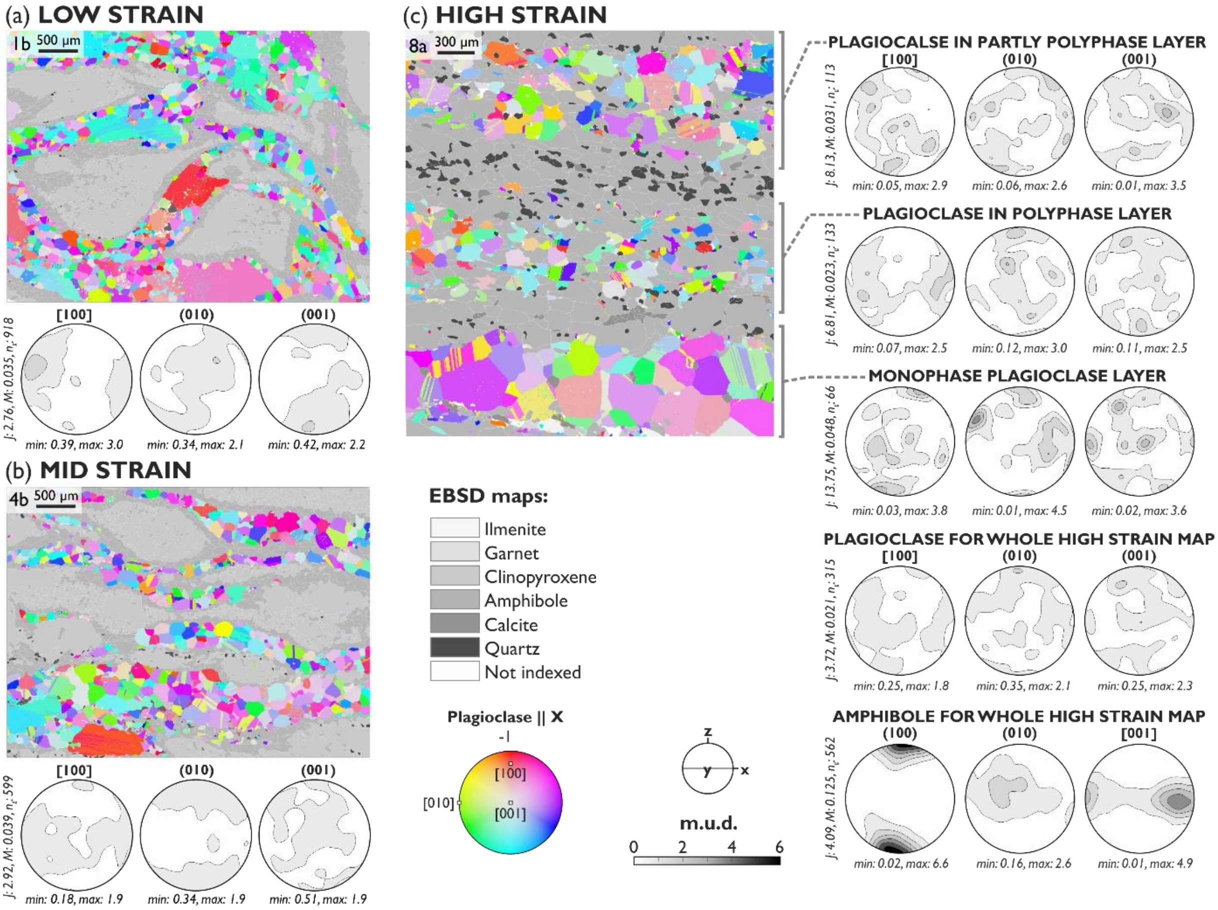

Figure 11: EBSD map and plagioclase CPO pole figures for representative (a) low, (b) mid and (c) high strain areas. EBSD maps show plagioclase orientations coloured parallel to the X direction, all other minerals are shown in grey. Pole figures showing plagioclase CPO, for (c), additional CPO are included for polyphase and monophase areas as well as the amphibole whole map CPO is also included (amphibole CPO for a and b are shown in Figure 9). All pole figures are equal area, lower hemisphere projections plotted as point per grain. J-index, M-index and number of grains (n_g) is shown for each set of pole figures.

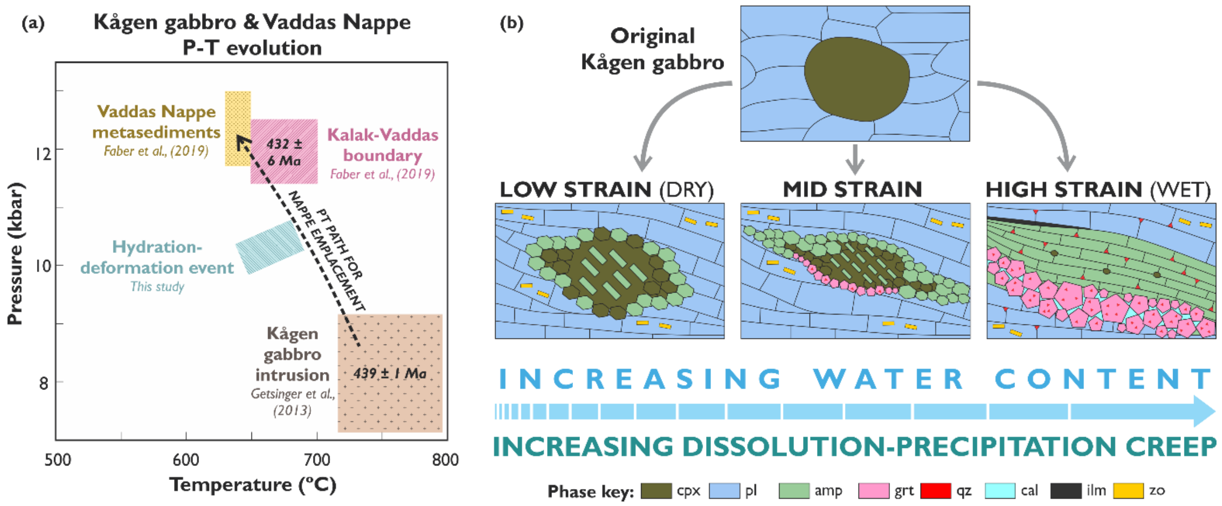

Figure 12: (a) Composite P-T-t evolution of Kågen gabbro and Vaddas Nappe utilising P-T estimates from this study for the hydration-deformation event, Getsinger et al. (2013) for the Kågen gabbro intrusion and Faber et al. (2019) for Vaddas Nappe metasediments and Kalak-Vaddas boundary. (b) Schematic diagram of the microstructural evolution of Kågen gabbro margins when deformation occurred under differing hydration conditions. The low strain example represents 'dry' conditions where the amphibole CPO is host-controlled and inherited from clinopyroxene. The high strain example represents fluid saturated conditions where the amphibole CPO is controlled by orientated growth.

Supplementary material for:

Dissolution precipitation creep as a process for the strain localisation in mafic rocks

Amicia L. Lee[1*], Holger Stünitz[1, 2], Mathieu Soret[2], Matheus Ariel Battisti[3]

[*]*amicia.lee@uit.no*
[1]*Department of Geosciences, UiT – Arctic University of Norway, Norway*
[2]*Institut des Sciences de la Terre (ISTO), Université d´Orléans, France*
[3]*Instituto de Geociências, Universidade Federal do Rio Grande do Sul, Brazil*

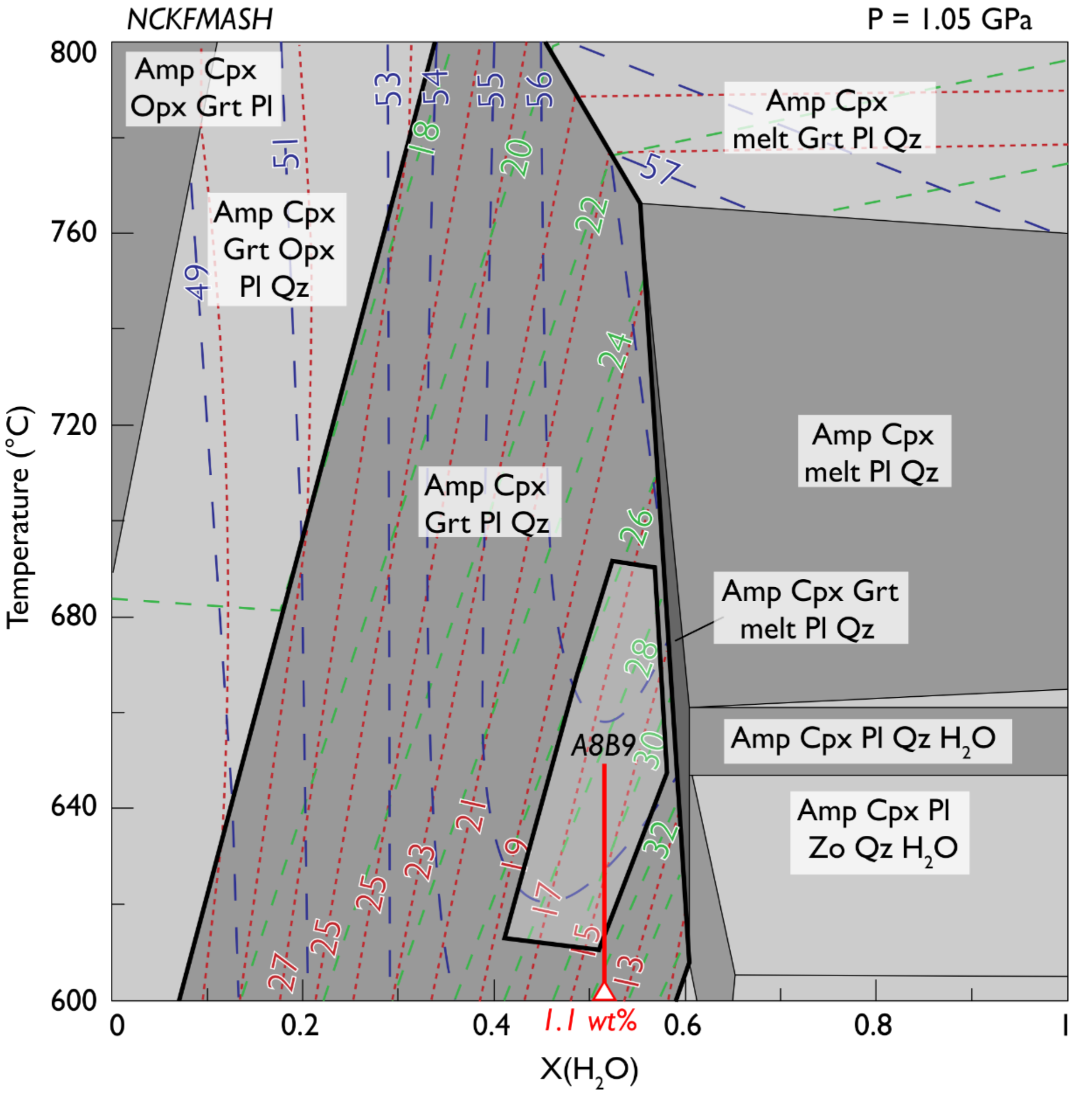

Figure S1: Temperature-X(H2O) phase diagram for the high strain areas of the Kågen gabbro margins. Pressure is fixed at 1.05 GPa and the calculate H$_2$O volume is 1.1 wt. %.

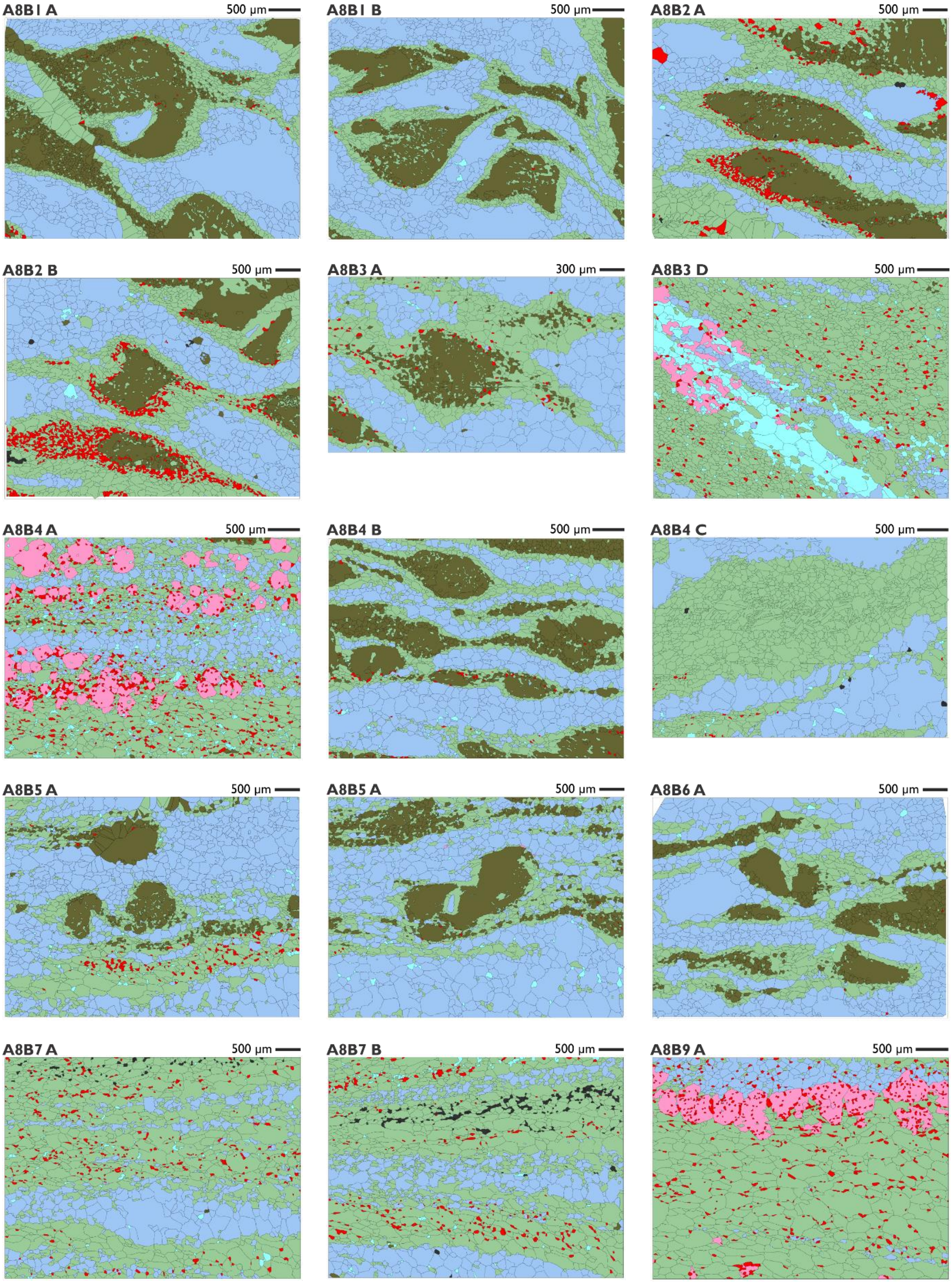

Figure S2: EBSD phase maps for all datasets used in this study. Data are displayed as grain maps that were calculated within MTEX. Phase key for all maps is displayed next to map A8B3 B.

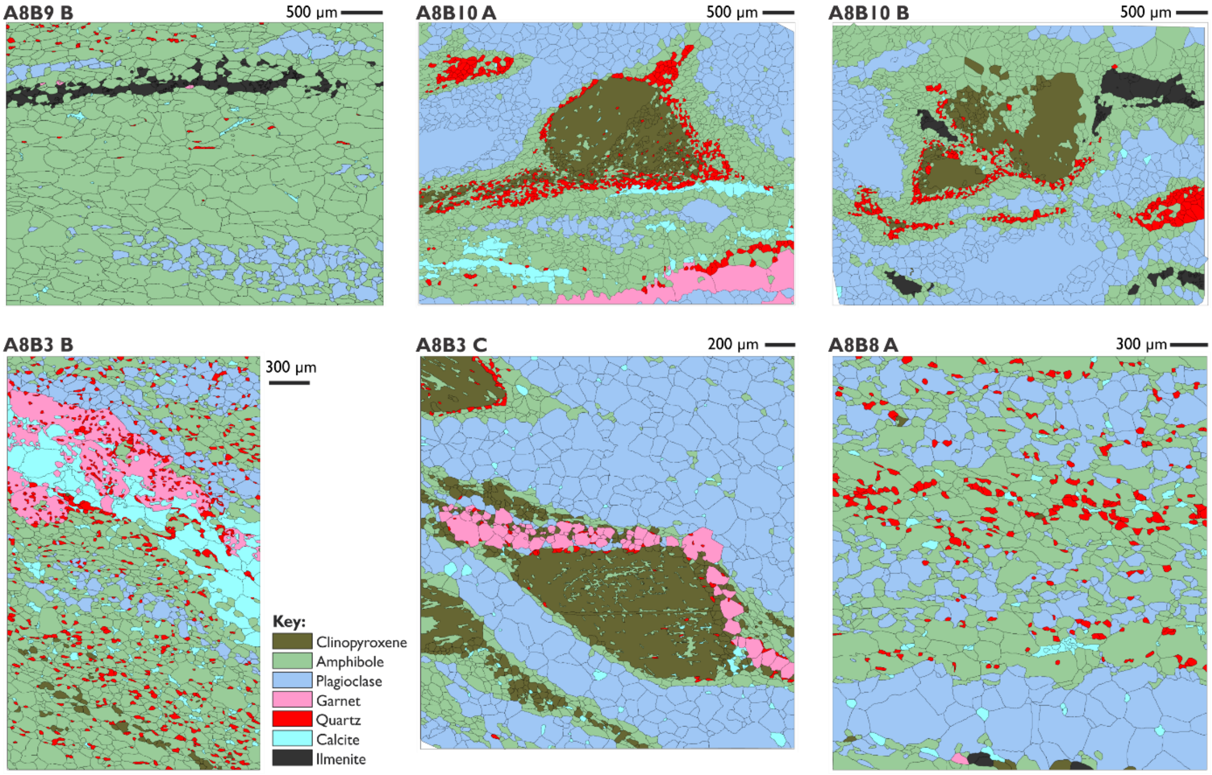

Figure S2 continued.

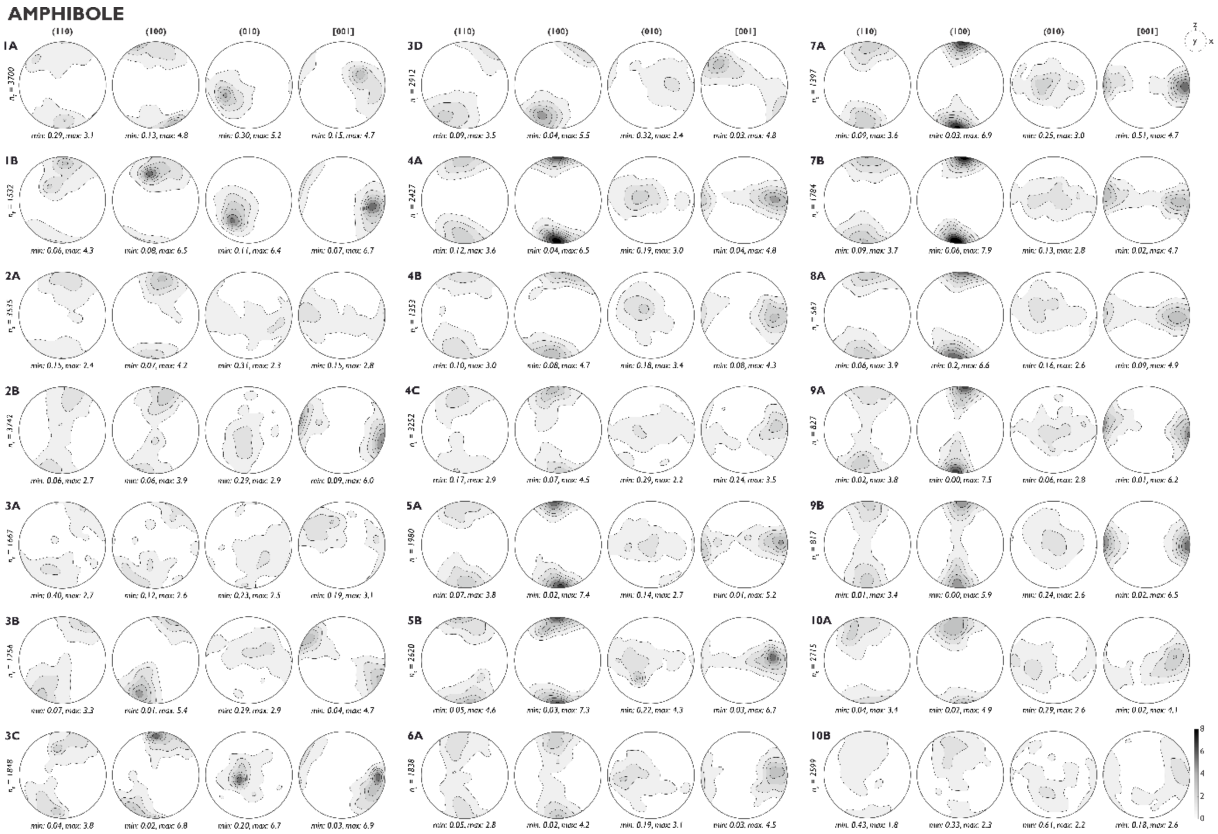

Figure S3: Point per grain, equal area, lower hemisphere amphibole CPO pole figures.

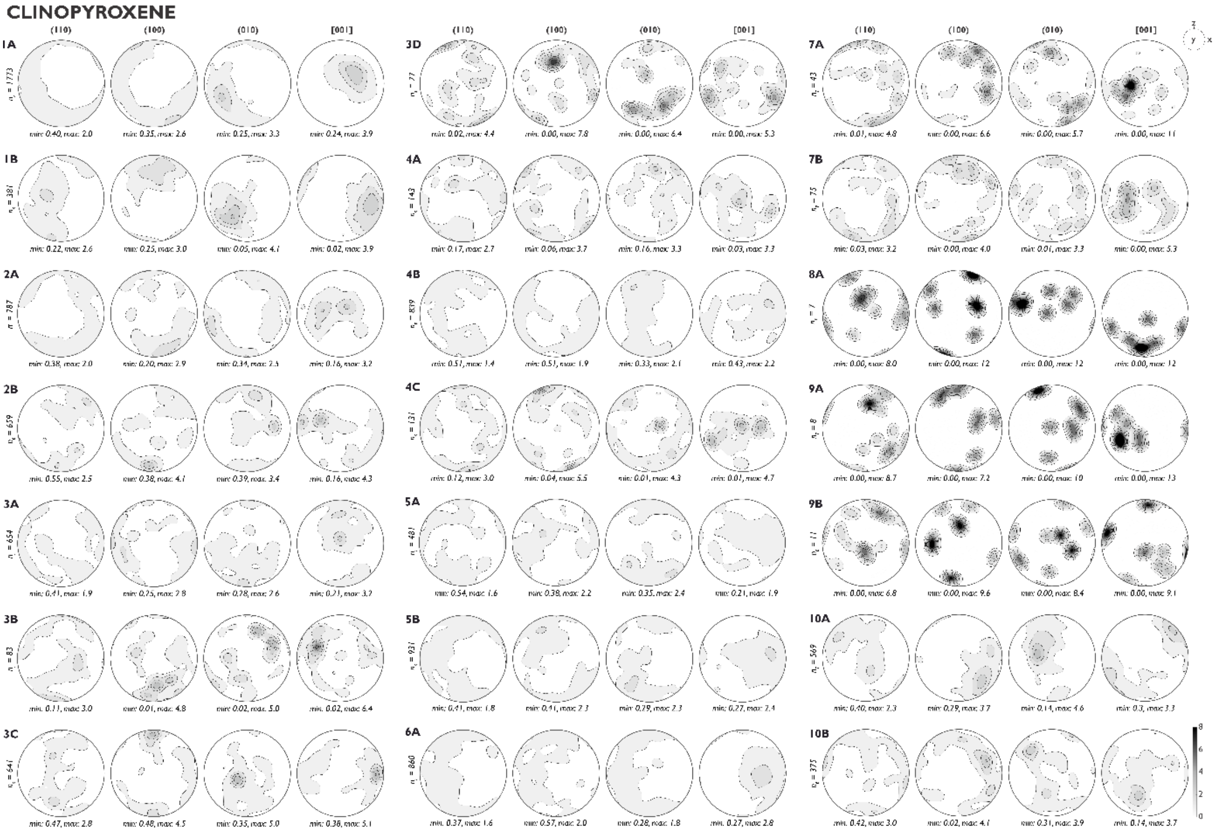

Figure S4: Point per grain, equal area, lower hemisphere clinopyroxene CPO pole figures.

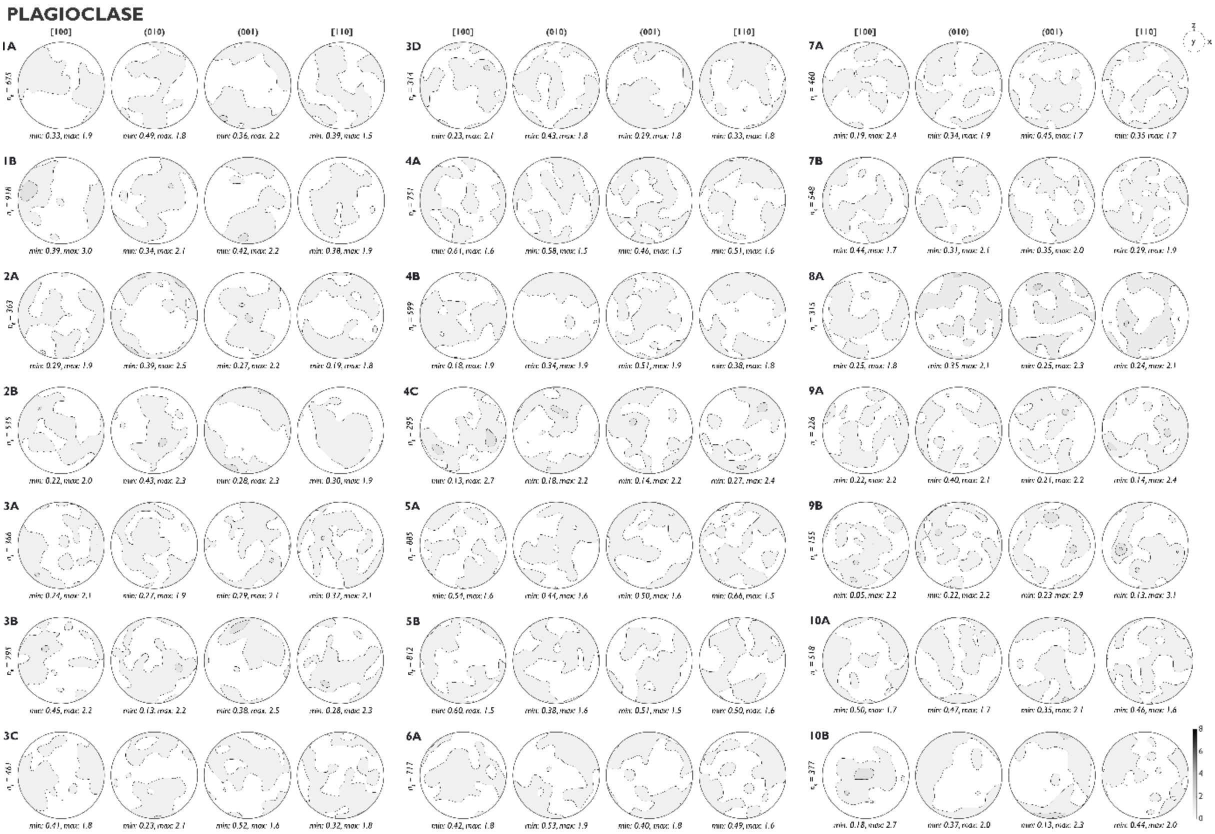

Figure S5: Point per grain, equal area, lower hemisphere plagioclase CPO pole figures.

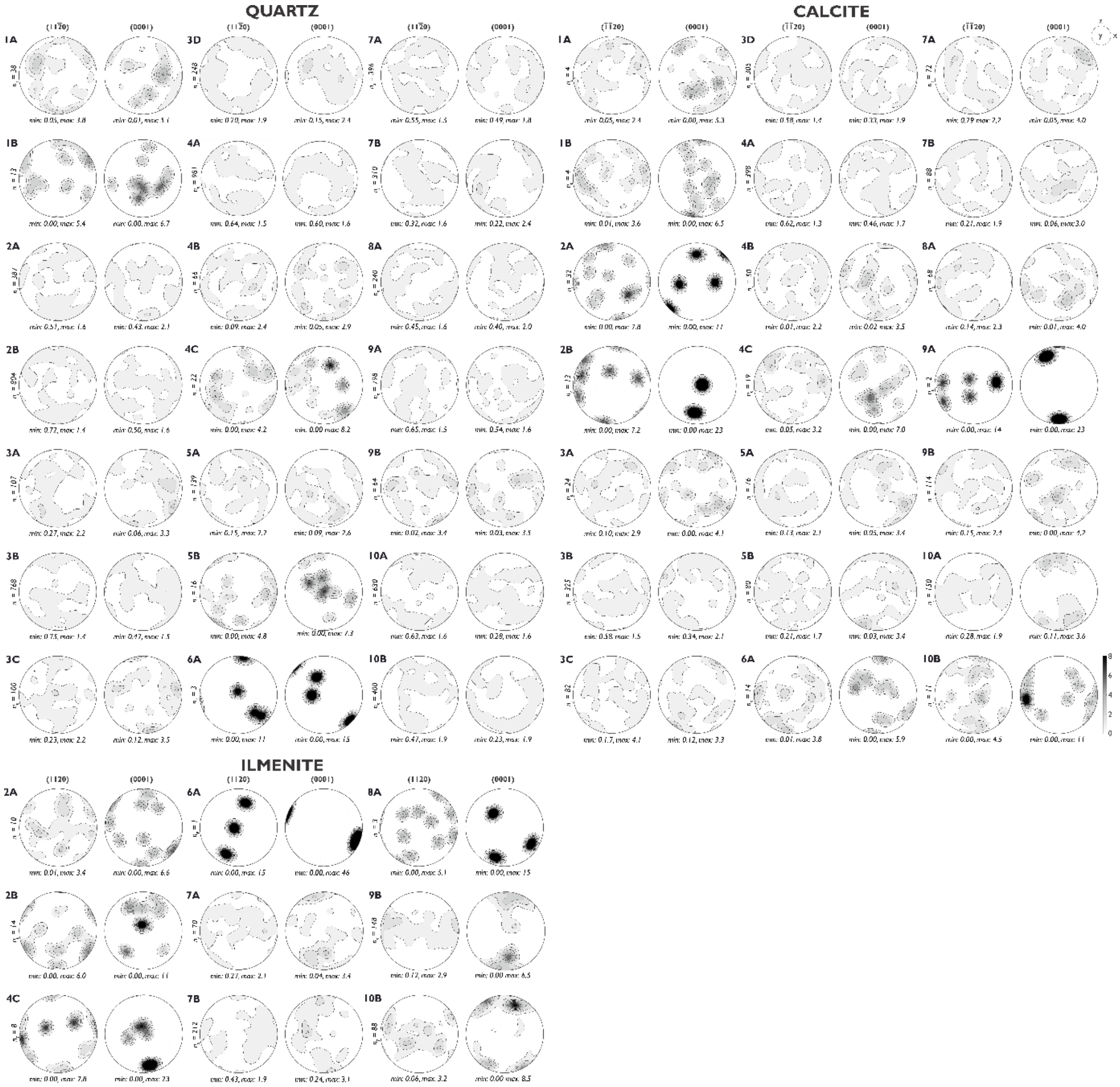

Figure S6: Point per grain, equal area, lower hemisphere CPO pole figures for quartz an ilmenite a<11-20> and c<0001> axes and calcite a<-1-120> and c<0001> axes.

Separate documents:

Table S1: Compilation of the P-T conditions calculated using the amphibole-plagioclase thermobarometry of Molina et al. (2015) and Holland and Blundy (1994) (see the method section of the manuscript for details).

Table S2: T conditions calculated at 1 GPa using the garnet-clinopyroxene thermometry of Powell (1985) and Krogh-Ravna (1988) (see the method section of the manuscript for details).